Thermal, Structural and Optical properties of $ZnFe_2O_4$ and $Ni_{0.6}Zn_{0.4}Fe_2O_4$ nanoparticles synthesized by a sol-gel method: Heterogeneous Fenton-like oxidation study

Elaziouti Abdelkader[1*], Laouedj Nadjia[2] and Benhadria Naceur[3]
1. Laboratoire des Sciences Technologie et Génie des Procédés L.S.T.G.P, Université des sciences et de la technologie d'Oran Mohammed Boudiaf (USTO M.B). BP 1505 El M'naouar 31000 Oran, ALGERIE
2. Laboratoire de Chimie des Matériaux Inorganiques et Application L.C.M.I.A, Université des sciences et de la technologie d'Oran Mohammed Boudiaf (USTO M.B). BP 1505 El M'naouar 31000 Oran, ALGERIE
*abdelkader.elaziouti@univ-usto.dz; elaziouti_a@yahoo.com

Abstract
Stable magnetically ferrospinels $ZnFe_2O_4$ (ZF) and $Ni_{0.6}Zn_{0.4}Fe_2O_4$ (NZF) nanoparticles (NPs) were successfully synthesized by a sol-gel method and characterized by XRD, SEM-EDX, UV-vis DRS and pH_{ZPC} technique. The as-prepared materials were investigated in the heterogeneous Fenton-like oxidation of Congo red dye. Results indicated that NZF crystallized in single-phase and exhibited smaller crystallite size (49 nm vs. 59.24 nm) than that of the pure ZF. The SEM analysis showed that the materials are elongated like shape.

NZF catalyst showed a red-shift of absorption bands and a more narrowed bandgap (2.30 eV vs. 1.65 eV) as compared to ZF. Urbach energy increased from 0.185 to 0.200 eV resulting in an increase in the Ni-content indicative of the fact that electrons encounter larger extent of disorder while transiting across the band gap. Under optimum conditions of 20 mg L^{-1} CR, 0.23 M H_2O_2, 1 g.L^{-1} catalyst, pH = 7.5 and 25 °C, up to ≈92% degradation efficiency could be achieved after 60 min of treatment. Kinetic studies confirmed that the heterogeneous Fenton-like processes followed pseudo first-order kinetics.

Keywords: $Ni_{0.6}Zn_{0.4}Fe_2O_4$, Congo red, Heterogeneous Fenton-like oxidation, Degradation efficiency, Synergy.

Introduction
In recent decade, the wastewater from the textile, dyeing, leather, pharmaceutical, paper, cosmetic, plastic and synthetic detergent industries, results in harmful effects to humans health as well as environment. Thus, wastewater treatment and recycling should be a major concern. One of the best and green environmentally friendly processes for the remediation of contaminated wastewater is advanced oxidation processes (AOPs).[75,95] These processes based on *in-situ* generation of highly reactive and non-selective hydroxyl radicals ($^{\cdot}OH$) are able to mineralize a broad range of refractory organic contaminants present in wastewater and groundwater systems.[24,44,58,72,76,78,97]

The generation of $^{\cdot}OH$ radicals is improved with conventional AOPs including: ozonation (O_3); a combination of ozone with UV irradiation (O_3/UV) or hydrogen peroxide (O_3/H_2O_2), or both (O_3/H_2O_2/UV); ozone combined with catalysts (O_3/catalysts); UV/H_2O_2; Fenton, Fenton-like and photo-Fenton processes (Fe^{2+}/H_2O_2, Fe^{3+}/H_2O_2 and Fe^{2+}/H_2O_2/UV) and UV irradiation, ultrasound and (or) high electron-beam irradiation and heterogeneous photocatalysis. In contrast, the non-conventional AOPs are the photo-electro-Fenton and sono-electro-Fenton processes.[12,26,28,43,45,83]

Homogeneous Fenton oxidation is reported as promising technology for the environmental remediation of various persistent, recalcitrant and non-biodegradable contaminants and has been intensively researched for several decades due to its high efficiency, relatively low cost, ease of application and mild reaction conditions of temperature and pressure.[68] However, the homogeneous Fenton process has significant drawbacks. Explicitly, (i) a narrow and low pH range (pH= 2–3), (ii) the production of massive amounts of hazardous iron sludge (iii) iron deactivation by the formation of complexing reagents such as phosphate ions and (iv) requirement of additional separation and disposal.[92]

Efforts to overcome the disadvantages related to the implementation of the Fenton type processes, heterogeneous Fenton and Fenton-like heterogeneous catalysts, generating hydroxyl free radicals with the aid of hydrogen peroxide, have been deployed.

The general requirements for heterogeneous Fenton catalysts are: (i) effectiveness at widespread ranges of pH and temperature (ii) high efficiency related to contaminant removal rates and H_2O_2 utilization, (iii) generation of little iron sludge and (iv) stability over long periods of application. However, many of these heterogeneous catalysts still operate under acidic conditions only and the generation of hydroxyl radicals is strongly affected by the hydrogen peroxide (H_2O_2) and ferric iron (Fe^{3+}) spicies leading to the obvious drop in degradation efficiency.[33]

The previous development of Fenton-like catalysts focosed on either single spinel ferrite materials such as Fe_3O_4, $CaFe_2O_4$, $CoFe_2O_4$, $MgFe_2O_4$, $NiFe_2O_4$, $EuFeO_3$, $BiFeO_3$, $SnFe_2O_4$, $ZnFe_2O_4$, MFe_2O_4 (M=Ni, Zn, Cu) or combined with other compounds as heterosystem including $ZnFe_2O_4$-reduced Graphene Oxide, MCM-41/Magnetite, $LiFePO_4$, Fe_2O_3/SBA-15, Fe/ZSM-5.[3,36,48,51,59,65,66,88,89,91,94] These

nanostructured spinel ferrite material containing ferric ions in the crystal lattice can proceed with the necessary redox reaction with adsorbed hydrogen peroxide molecules to generate highly oxidizing hydroxyl free radicals for oxidative removal of organic pollutants.[49]

It has been reported that Zinc ferrite or franklinite ($ZnFe_2O_4$) is a normal spinel structure with Zn^{2+} ions situated at the tetrahedral (A) sites, whereas Fe^{+3} ions at the octahedral (B) sites[17] located in a network of oxygen ions with FCC arrangement.

Recently, $ZnFe_2O_4$, with a typical band gap Eg of about 1.9 eV (λ_{max} =653 nm)[56], has potential application as the Fenton-like heterogeneous catalysts in the oxidation processes of refractory contaminant. However, due to their low valence band potential and poor quantum efficiency, $ZnFe_2O_4$ cannot be used directly in the photocatalysis processes.[80] In view of better, safe and sustainable utilization of solar energy by photocatalysts, two approaches have been proposed either for size-controlled synthesis of various functional nano-materials such as transition metals doping[9,11,32,34,63] or for effective photoinduced electron–hole pair's separation, including semiconductor combination with matching band potentials.[13,15,16,40,41,81,87,96]

It is worthwhile to note that these catalysts based iron-containing compounds when used directly in solution, often give rise to particle agglomeration with severe loss of effective surface area due to the magnetic interactions. Moreover, doping with transition metal such as Ni^{+2}, Mn^{+2}, Co^{+2} and Cu^{+2} into the spinel $ZnFe_2O_4$ nanostructures, could be able to control the particle size, to efficiently avoid particles from agglomeration and to hence improve the structural, morphological, magneto-optical and heterogeneous Fenton-like activity. Among the nanostructured spinel ferrite materials, Nickel-Zinc ferrites ($Ni_xZn_{1-x}Fe_2O_4$) are considered as one of the most versatile soft ferromagnetic material because of its high resistance, high saturation magnetization and low eddy current losses.[69]

Mixed Ni–Zn ferrite has attracted a great interest due to their potential applications in microelectronics, magneto-optics, as microwave device components, catalysts, photo-catalysts, gas sensors, absorbent materials, information storage and electronic devices and photoelectrochemical water splitting and biomedical applications.[27,30,31,47,52,75]

The general formula of Ni-Zn ferrite is $[Fe_{1-x}^{3+}Zn_x^{2+}]^{tet}[Ni_{1-x}^{2+}Fe_{1+x}^{3+}]^{oct}O_4$ in which the tetrahedral (A) sites of the lattice structure are occupied by $[Fe_{1-x}^{3+}Zn_x^{2+}]$ ions and the octahedral sites (B) are occupied by $[Ni_{1-x}^{2+}Fe_{1+x}^{3+}]$ ions in the spinel formula AB_2O_4. Up to now, various synthetic methods have been developed to prepare Ni-Zn ferrite nanoscale particle such as solvothermal, coprecipitation, hydrothermal, citrate precursor, sol–gel, self-propagating high-temperature method and microwave combustion method.[18,53-55,82,85,93]

However, the above methods have some disadvantages such as high-energy consuming, need of complicated equipment, requirement of a strong base, higher processing temperature and also require rather long reaction time caused by the multiple steps to complete the crystallization of final product. Recently, sol-gel method has gained much importance for the preparation of such functional nano-ferrites.[8,38,73] Generally speaking it gives inorganic high purity materials at mild synthesis conditions.[24]

On the other hand, the use of the Fenton-like heterogeneous catalysis in the oxidation of organic as pollutant using Ni-doped $ZnFe_2O_4$ nano-catalysts prepared by sol-gel route is less explored.

Therefore, in the present study, two types of ferrite materials: $ZnFe_2O_4$ (symbolized by ZF) and $Ni_{0.6}Zn_{0.4}Fe_2O_4$ (symbolized by NZF) were successively synthesized by a simple sol-gel method. The as-prepared Nickel-Zinc ferrite catalysts were in detail characterized by X-ray diffraction (XRD), Scanning electron microscopy (SEM) and UV-vis diffuse reflectance (UV-vis-DRS) technique. The impact of Ni-content (x) on the structure, morphology and optic properties of NZF was studied. The heterogeneous Fenton-like activity of NZF catalysts were investigated in the oxidation of Congo red azo dye, as a probe pollutant, from aqueous solution along with H_2O_2.

We have also explored systematically the effects of the operational parameters such as initial pH solution, H_2O_2 concentration, initial dye concentration, catalyst dosage, temperature of the system and inorganic salt. The degradation reactions were correlated with the pseudo-first-order kinetic model. On the basis of their structural, morphological and optical features, a possible mechanism of the increased heterogeneous Fenton-like activity of NZF catalyst was elucidated in details.

Material and Methods

$FeSO_4$ $7H_2O$ (99.99%, Sigma Aldrich), Zn $(COO)_2$ $6H_2O$ (99.99%, Sigma Aldrich), $NiCl_2$ $6H_2O$ (99.99, Sigma Aldrich) and Citric acid (99.99%, Sigma Aldrich). Congo red; 1-naphthalene sulfonic acid, 3, 30-(4,40-biphenylenebis (azo)) bis (4-amino-) disodium salt) is a benzidine-based anionic diazo dye, that is, a dye with two azo groups ($C_{32}H_{24}N_6O_6S_2.2Na$). Distilled water was used for preparation of various solutions. The molecular structure and physicochemical properties of Congo red dye are presented in table 1.

Polycriystalline spinel ferrite with formula $Ni_{0.6}Zn_{0.4}Fe_2O_4$ (is denoted as NZF) was prepared via the citrate method by dissolving stoichiometric amounts of $FeSO_4$ $7H_2O$, Zn $(COO)_2$ $6H_2O$ and $NiCl_2$ $6H_2O$ with the molar ratio of Ni^{+2} : Zn^{2+}: Fe^{3+} = x:1-x:2 in distilled water and adding them to an aqueous solution of citric acid (a molar ratio of the metals to citric acid (M:CA of 1:2) under continuous stirring.

Table 1
Chemical structure and physicochemical properties of Congo red dye

Molecular structure	Chemicals properties	
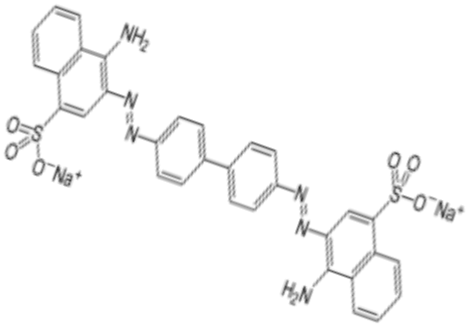	Molecular formula	$C_{32}H_{22}N_6Na_2O_6S_2$
	Absorption wavelength (nm)	497
	Chemical class	Diazo dye
	Molecular weight ($g.moL^{-1}$)	696.665
	Molecular surface area ($Å^2$)	557.6
	Density ($g.cm^{-3}$) at 25°C	0.995
	Dye class used for food	Azo
	Melting point	>360°C
	Color	Blue (pH= 3.0) to Blue red (pH=5)
	pKa	3-4.1

The mixture was then stirred until the obtained solution became brown red and was kept under stirring at room temperature for 24 hours and the precipitate was finally collected, washed with deionized water and ethanol for three times and was then dried at 80 °C for 24 h. Finally, the precursor was consequently milled and calcined at T=900 °C for 4 hours with the heating rate of 10 °C. For comparison purpose, ZN (stands for $ZnFe_2O_4$) was also prepared in the similar route by calcination ZN particles at T=1000 °C for 4 hours.

The crystal structures of ZF and NZF samples were analyzed by Bruker D8 Advance XRD with Cu-Kα radiation (λ = 0.154178 nm) for 2θ over 10°-80° and a scanning rate of 10°/min. The average crystallite size of the synthesized catalysts is calculated from the full-width-half-maximum (FWHM) of the diffraction peaks using Scherrer equation (Eq. 1):[4]

$$\mathbf{d_{DRX} = \frac{0.9\,\lambda}{\beta \sin\theta}} \qquad (1)$$

where d_{XRD}, λ, β and 2θ are the average crystallite size of the phase under exploration, the X-ray wavelength (1.5406 Å), the full-width at half maximum FWHM of the peaks in radians and Bragg angle in radians.

The size and the morphologies of the sample were examined using Jeol JSM 6360 LV Scanning Electron Microscope. UV–vis spectrophotometer (Perckin Elmer Lambda 650) equipped with an integrating sphere to determine the UV–vis diffuse reflection spectra in the wavelength range 200–900 nm. The band gap energy of the samples can be determined from Kubelka-Munk (K-M) model.[14] The residual pollutant concentrations during degradation were monitored with UV mini-1240 Spectrophotometer (Shimadzu UV mini-1240) using 1 cm optical pathway cells.

The heterogeneous Fenton–like experiments were performed in 400 mL glass beaker. For the reaction experiment, 0.1 g of catalyst (i.e. ZF and NZF) was added to 200 mL of CR dye aqueous solution at an initial concentration of 20 $mg.L^{-1}$ followed by adjusting pH between 7 and 8. Before oxidation, the suspension was magnetically stirred for 60 min in the dark until the adsorption equilibrium was reached. After that, an aliquot of hydrogen peroxide (H_2O_2) with H_2O_2/H_2O volume ratio ranging from 2.5 to 30 was added to the solution to initiate the reaction.

At given intervals, 5 ml aliquots were collected and filtered. The filtrates were finally monitored using a UV–vis spectrophotometer (Shimadzu UV mini-1240) at the maximum absorption band of CR (λ_{max} =497 nm). The data obtained from the catalytic degradation of CR experiments were then used to calculate the efficiency of the catalyst η' (%) of the substrate (Eq. 2):

$$\mathbf{\eta'(\%) = [\frac{(C_i - C_f)}{C_i}]\,100} \qquad (2)$$

where C_i is dye initial concentration ($mg{\cdot}L^{-1}$) and C_f is dye residual concentration after certain time intervals ($mg\ L^{-1}$).

According to the Planck's Law, the absorption wavelength λ is related to the band gap E_g of the material (Eq. 3):

$$\mathbf{E_g = \frac{1239}{\lambda}} \qquad (3)$$

The following Langmuir–Hinshelwood model was used to study the kinetics of the process (Eq. 4):

$$\mathbf{\ln\frac{C_0}{C} = K_{app}t} \qquad (4)$$

where k_{app} is the apparent pseudo-first order rate constant, C_0 and C are respectively the concentration at t=0 and t. The plot of ln C_0/C against t should give straight lines whose slopes are equal to K_{app}.

The half-life of dye degradation at various process parameters was raised from eq. 5:

$$t_{1/2} = \frac{0.693}{K_{app}} \quad (5)$$

where $t_{1/2}$ (half-life time) is defined as the amount of time required for the heterogeneous oxidation of 50% of CR dye.

Results and Discussion

Structural and FT-IR Analysis: Typical XRD patterns of spinel ZF and NZF samples are depicted in fig. 1. The diffraction peaks are the reflections corresponding to the hkl planes (111), (220), (311), (222), (400), (422) and (511). These diffraction peaks confirm the formation of cubic spinel structure of crystal (space group Fd-3m and JCPDS CARD 01-1108). There is no other peak which indicates that the samples crystallize in single-phase cubic structure. It can be seen from the compiled results, as illustrated in fig. 1 and table 2, that the decrease in intensity of peaks associated with the shift of their positions to higher values of 2*θ*, were observed in the XRD patterns of NZF, indicative of the decrease in the lattice parameter for the cubic NZF sample with Ni-content (x=0.6). Based on the Scherrer's equation (Eq. 1), the average crystallite size (d_{XRD}) was calculated from the FWHM using the broadening of the hkl = 311, as prominent reflection peak. The calculated average crystallite size of both samples is tabulated in table 2.

It was found that the crystallite size of undoped ZF is 59.24 nm and it was decreased to 49.00 nm with increasing the Ni-dopant (NZF). It is usually known that crystallite size (d_{XRD}) of a sample is inversely proportional to the FWHM, indicating that a broader peak represents smaller nanoparticle sizes.[37] The main reason responsible for the increased crystallite size of NZF sample could be explained by the Ni-content (x=0.6). It can significantly affect the decrease of ZF crystallinity in NZF material by acting as a grain growth inhibitor of ZF.[67] The lattice constants "*a*" of the samples, calculated from their corresponding XRD pattern data using Fullprof program, are displayed in table 2.

From the observed results, it was found that lattice parameter values decreased from 8.4404 Å (ZF NPs) to 8.3857 Å (NZF NPs) with increase in the Ni-dopant (x=0.6), in accordance with gradual substitution of Zn^{2+} ions of larger ionic radius (0.83 Å) in ZF spinel by smaller ionic radius (0.74 Å) of Ni^{2+} ions in N-doped ZF (NZF)[60,70,71,78] and decrease in the concentration of O vacancies, which leads to lattice contraction. The lattice parameter "*a*" is in good agreement with the standard JCPDS value of 8.441 Å (JCPDS No. 22-1012). The X-ray density (D_t) was calculated using the equation (Eq. 6):

$$D_t = \frac{Z\ M_c}{a_{exp}^3\ N} \quad (6)$$

. **Table 2**
Crystallographic parameters of the spinel ZF and NZF nano-catalysts

Abbr.	Catalysts	Ni-content	2θ (degree)	a (Å)	FWHM (radians)	d_{XRD} (nm)	D_t ($g.cm^{-3}$)	SSA ($m^2.g^{-1}$)
ZF	$ZnFe_2O_4$	0	35.2380	8.4404	0.1407	59.24	5.325	19.02
NZF	$Ni_{0.6}Zn_{0.4}Fe_2O_4$	0,6	35.4754	8.3857	0.1664	49.00	5.338	22.94

Abbr.: Abbreviation

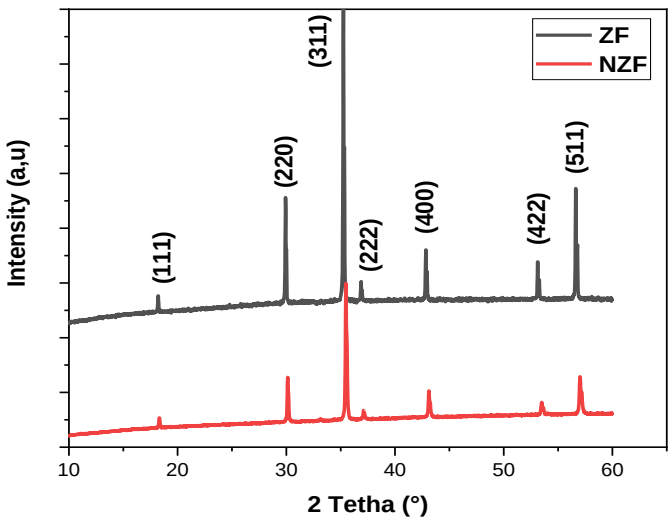

Fig. 1: X-ray diffraction patterns of ZF and NZF nano-catalysts

where Z is the number of chemical species in the unit cell of spinel lattice (z=8), Mc is the molecular weight of the sample (g mol^{-1}), a_{exp} is the experimental lattice parameter of the ferrite (Å) and N is Avogadro's number (6.022×10^{23} mol^{-1}). The X-ray density (D_t) depends on the lattice constant and molecular weight of the sample. The X-ray density *Dt* as a function of Ni-content (x) is reported in table 2. It can be seen from the table 2 that the X-ray density (D_t) increases from 5.325 to 5.338 $g.cm^{-3}$ as the Ni-content (x) varies from x=0 to x= 0.6.

Assuming that the particles have spherical shape and uniform size, the specific surface area average particle size can be estimated by Brunauer, Emmett and Teller (BET) formula (Eq. 7):

$$S_s = \frac{6}{D_t d_{XRD}} \quad (7)$$

where d_{XRD} (nm) is the average particle sizes of magnetically ferrospinels and D_t is their corresponding X-ray density. It can be observed from table 2 that the specific surface area increases from 19.02 $m^2.g^{-1}$ (ZF NPs) to 22.94 $m^2.g^{-1}$ (NZF NPs) as the Ni-content (x) increases from x=0 to x= 0.6, in perfect harmony with an inhibition of crystallite nucleation and retardation of crystallite growth processes (to prevent the construction to larger clusters).

Morphological and Elementary Analysis: The morphologies and structures of the magnetically ferrospinel NZF NPs were investigated using SEM images (Fig. 2). Typical low-resolution SEM images as seen in fig. 2a-b, clearly reveals that NZF consisted of large randomly shaped aggregates of smaller individual ultrafine NPs. Groups of ultrafine particles assemble into bigger particles with size up to 500 nm. As the particles are very small, so they get aggregated to certain extent due to high surface-to-volume ratio as well as magnetic interactions.

Fig. 2c displayed EDX analysis pattern of NZF nano-catalyst only. The relative atomic abundance of Fe, Zn, Ni and O elements present in the uppermost surface and bulk layers of NZF are reported in table 3.

These results revealed that NZF nano-catalyst was successfully prepared and the surface O/Fe ratio (2.6) is slight higher to the bulk O/Fe ratio that is 2, indicating that the samples have intrinsic defect (as mentioned in XRD analysis), which are usually presented in impurity and dopant-controlled regimes of slightly sub-stoichiometric pure or transition metal doped metal oxides such as TiO_2, WO_3 and CeO_2. Basically, intrinsic oxygen vacancy defects in NZF NPs sample provide much more surface active sites for the adsorption of organic contaminants. A finding is crucial for the adsorption and the heterogeneous Fenton-like degradation process by providing large contact surface areas with the organic contaminants and offering high percentages of reactive sites surface atoms for catalyzation for the adsorption.

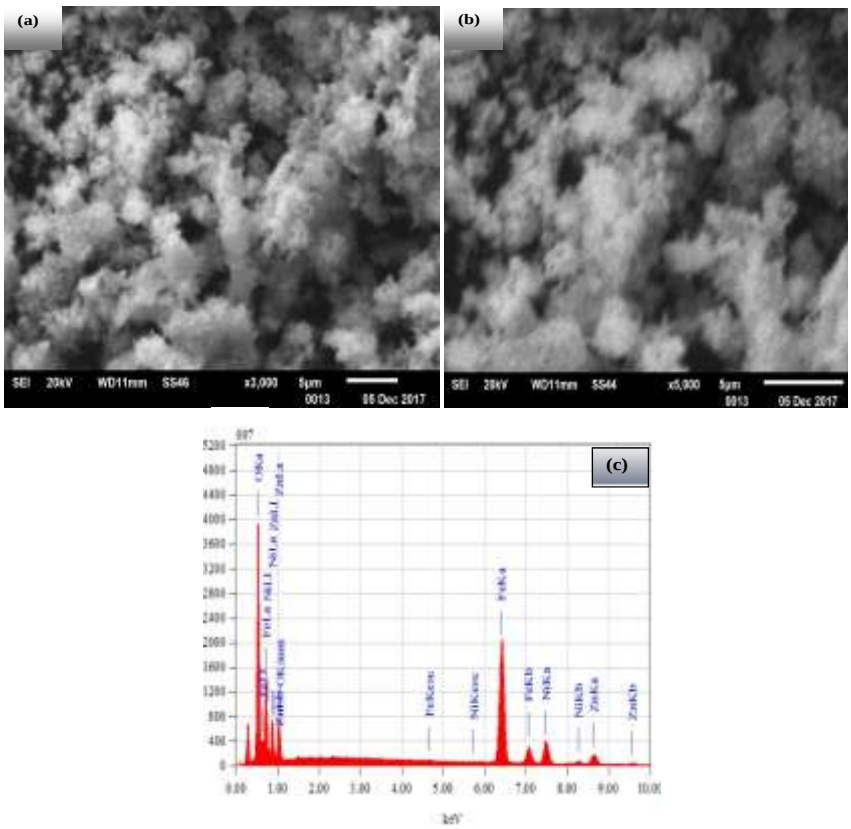

Fig. 2: Micrography SEM for NZF nano-catalyst: (a-b) Low-resolution (c) EDX spectrum of NZF nano-catalyst

Table 3
The atomic abundance (surface and bulk) of elements measured for the ZNF nano-catalyst

Elements	Mass (%)	Atome (%)	Surface O/Fe ratio
O	33.41	64.33	2.62
Fe	44.59	24.59	
Ni	13.32	6.99	
Zn	8.68	4.09	

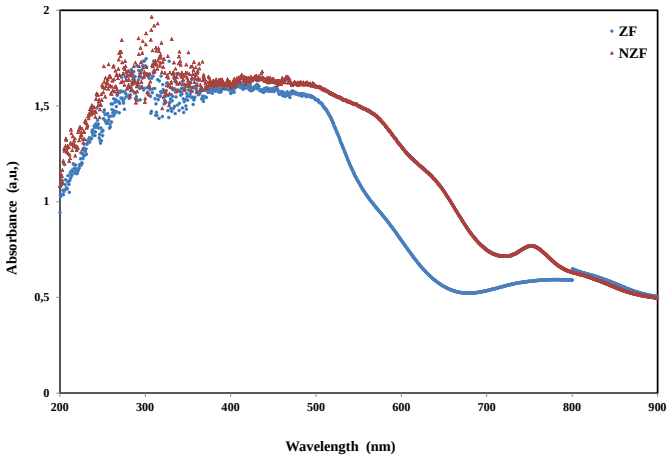

Fig. 3: DRS spectra of ZF and NZF nano-catalysts

Ultraviolet–Visible Analysis : The optical absorption properties of the spinel ZF and NZF nano-catalysts were investigated by UV-Vis-DRS. As depicted in fig. 3, the pristine ZF sample shows a high absorption band in 200–600 nm region which is typical to ferrite based Nano systems which may have orbital contributions from 3d4-4s1, 3d5 and 4S.[29,77] ZF and NZF nano-catalysts exhibit a well-defined absorbance edges in the visible region at 600 nm and 780 nm respectively which give the first notation that both catalysts can be efficiently used as a visible light responsive photo-catalyst. The band structure is generally defined by taking the *O2p* orbital as the VB and the Fe3d orbital as the CB. The absorption of ferrospinels in the visible light region is due to the electron excitation from *O2p* into the *Fe3d* level.

Compared with the absorbance edges of ZF, the absorption edge of NZF nano-catalyst have red shifted, which might be ascribed to the increase the crystalline defects and thus additional band gap energy levels between the VB and CB. These localized levels (oxygen vacancies) in the photocatalyst allow the excitation of electrons from the VB to CB with the absorption of relatively low energy photons.

Moreover, presence of two absorption edges in UV-vis-DRS spectrum of NZF has been correlated to two crystallite phases belonging to NZF catalyst[61]. The energy band gap (Eg) was then calculated from the plot of the modified K-M function as in the equation (Eq. 8):

$$\alpha h\nu^{1/n} = \beta(h\nu - E_g) \quad (8)$$

where α, h, ν, Eg and β are the linear absorption coefficient, Planck's constant, light frequency, band gap energy of the material and a constant involving property of the bands respectively. The exponent of *n* is the power factor of the transition mode which is dependent upon the nature of the material, whether it is crystalline or amorphous. The band gap values were calculated using the Tauc plotting of $(\alpha h\nu)^2$ vs. hν and $(\alpha h\nu)^{1/2}$ vs. hν for indirect and direct transitions respectively by extrapolating the straight line of these plots to $(\alpha h\nu)^2 = 0$ and $(\alpha h\nu)^{1/2} = 0$ as indicated in fig. 4 and fig. 5, respectively.

The estimated band gap values for ZF and NZF are listed in table 4. To verify the optical band transition mode, whether it is direct or indirect for our present ZF and NZF nano-catalysts, one can use eq. 9 which can be rearranged as follows[7]:

$$Ln(\alpha h\nu) = Ln\beta + nLn(h\nu - E_g) \quad (9)$$

Hence, plotting of Ln (αhν) vs. Ln (hυ-Eg), gives a straight line whose slope determines the power factor (n) (Fig. 6), indicating that the empirical equations of this linear relationship are given by the following expressions eq. 10 and eq. 11:

$$\text{For ZF; } Ln(\alpha h\nu) = 4.73 + 1.99Ln(h\nu - E_g)\,;\ n = 2 \quad (10)$$

$$\text{For NZF; } Ln(\alpha h\nu) = 0.53 + 0.88Ln(h\nu - E_g);\ n = 0.88 \quad (11)$$

The calculated values of the transition power factor (n) of ZF and NZF matrix are found to be 2 and 0.5 respectively as tabulated in table 4. Thus, for non-crystalline and crystalline materials, indirect and direct transitions are effective for ZF and NZF nano-catalyst according to Tauc's relation[78].

Based on the above reported results (Table 4) for indirect transition, the band gap of 2.30 eV was obtained for ZF while the value of 1.65 eV was found for direct transition corresponding to NZF. Comparison of these values with the reported values for bulk $ZnFe_2O_4$ (1.9 eV) confirms blue shift for obtained band gap potentials of both ZF and NZF nano-catalysts due to quantum confinement effect and the reduction of structural defects. However, the abundant surface and interface defects in the agglomerated nanoparticles were supposed to be responsible for the red-shift of absorption edge of NZF as compared with the corresponding value for the pristine ZF (2.30 eV).[39,50]

The width of the localized states available in the optical energy gap of the films affects the optical band gap structure and optical transitions and it is called Urbach tail, which is related directly to a similar exponential tail for the density of states of either one of the two band edges. According to Urbach effect[79], an increase of doping concentration would induce the formation of band tails in the band gap which is expressed by eq. 12:

$$\alpha = \alpha_0 e^{\frac{h\nu}{E_U}} \qquad (12)$$

where α_0 is a constant, hυ is the photon energy and Eu is the Urbach energy, which refers to the optical transition between occupied states in the VB tail and the CB edge. Urbach energy is estimated by plotting Ln(α) vs. hv and fitting the linear portion of the curve with a straight line. The reciprocal of the slope of this linear region yields the value of Eu. These values are reported in table 5 and fig. 7.

Table 4
Approximated allowed indirect and direct band gaps of ZF and NZF nano-catalysts

n	Band gap energies; Eg (eV)	
	ZF	NZF
1/2	1.90	1.65
2	2.30	1.95

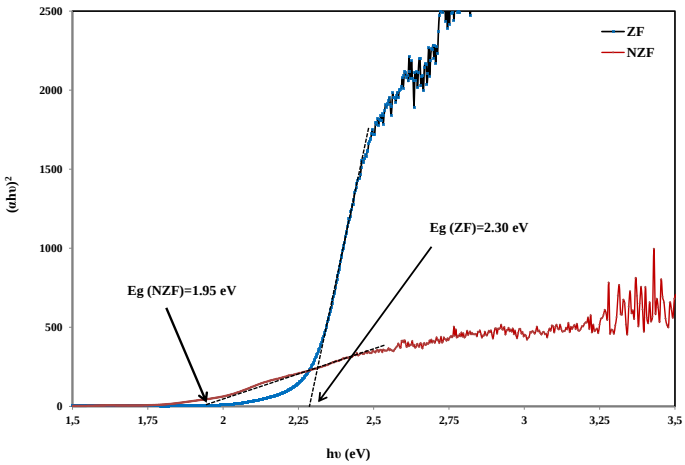

Fig. 4: $(\alpha h\nu)^2$ versus hv ploting of ZF and NZF nano-catalysts

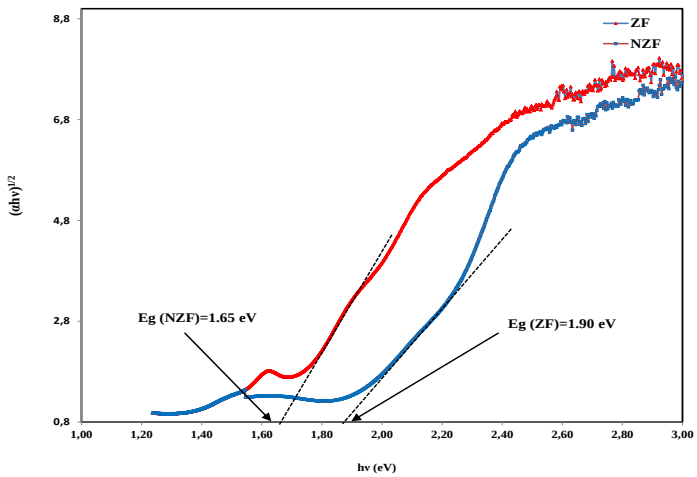

Fig. 5: $(\alpha h\nu)^{1/2}$ versus hv ploting of ZF and NZF nano-catalysts

From this plot it is evident that Eu increases with increasing the Ni-content x from 0 to 0.6, an increase of the disorder appears from 0.185 to 0.200 eV with increasing the Ni-content x from 0 to 0.6 indicative of the fact that electrons encounter larger extent of disorder while transiting across the band gap. This highlights that the behavior of optical energy gap is matching with the behavior of Urbach energy. This increase is due to increased acceptor levels of interstitial oxygen atoms. The obtained results were found to be in good agreement with those of literature[35]. Furthermore, the valence and conduction band edge energy[90] of a semiconductor can be assessed through the following empirical formulae eq. 13 and eq. 14:

$$E_{VB} = \chi - E_e + 0.5E_g \quad (13)$$
$$E_{CB} = E_{CB} - E_e \quad (14)$$

where χ is the absolute electronegativity of the semiconductor, which is the geometric mean of the electronegativity of the constituent atoms. Herein, the electronegativity of an atom is the arithmetic mean of the atomic electron affinity and the first ionization energy; E_e is the energy of free electrons on the hydrogen scale (about 4.5 eV), E_g is the band gap of the semiconductor; E_{CB} is the conduction band potential and E_{VB} is the valence band potential. The *X* values for ZF and NZF are 5.437 and 5.177 eV respectively. Thus, the E_{VB} of ZF and NZF are estimated to be 2.087 and 1.502 eV and their corresponding E_{CB} are -0.213 and -0.148 eV (vs. NHE).

The pH of zero point charge or pH $_{ZPC}$: Zeta potential (i.e. the isoelectric point, or IEP), an indicator of any dispersion stability, is influenced by the surface chemistry which can be changed by any number of means including a change in the pH, salt concentration, surfactant concentration and other formulation options. An isoelectric point measurements study how pH influences zeta potential. The pH $_{ZPC}$ of NZF NPs catalyst was determined by the pH drift method. The pH of a solution of 0.01 M NaCl was adjusted between pH 4 and pH 10 by adding either HCl or NaOH. Then, 0.15 g of NZF NPs powder was added to 50 mL of the solution and the final pH (pH_f) was measured after 48 hours.

The pH_{ZPC} is defined as the point where the electrical charge density on the surface of the nanoparticles is zero. The ΔpH versus pH_i plot for NZF is illustrated in fig. 8. The pH_{ZPC} of NZF NPs was determined to be 6.75, which is consistent with reported value of pH 6.4 implying that they are positively charged under acidic and neutral pH conditions (<6.75) but become negatively charged at pH values above 6.75.

Table 5
n, χ, λ_{max}, Eg, Eu, E_{VB} and E_{CB} for ZF and NZF nano-catalysts

Abbr.	Catalysts	n	χ (eV)	λ (nm)	Eg (eV)	Eu (eV)	E^0_{CB} (eV)	E^0_{VB} (eV)
ZF	$ZnFe_2O_4$	2	5.437	539	2.30	0.185	-0.213	2.087
NZF	$Ni_{0.6}Zn_{0.4}Fe_2O_4$	1/2	5.177	751.51	1.65	0.200	-0.148	1.502

Abbr.: Abbreviation

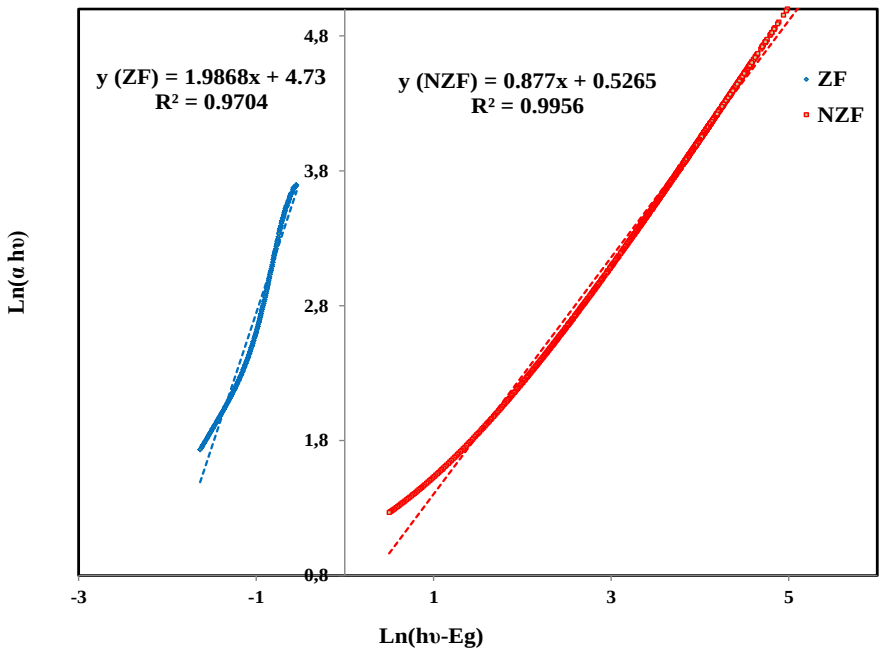

Fig. 6: Representation of Ln (a hυ) against Ln (hυ-Eg) for ZF and NZF nano-catalysts

Heterogeneous Fento-like oxidation of Congo red azo dye: Fig. 9 illustrated UV-visible spectra of CR in aqueous solution at various pH solutions. In aqueous medium, CR exhibited an absorption band at 497 nm (π→π*) and 347 nm (n →π*) transition associated with the azo group. As seen in fig. 9, the CR monomers have nearly constant absorption bands and absorbance intensities over a range of pH values of 6 to12, while they are most sensitive to the pH solution under acidic medium (pH<6). The main band of CR monomeric species (497 nm) gradually shifted to the longer wavelengths, almost reaching 595.5 and 537.5 nm at pH 2 and 4 respectively. The bathochromic shifts (J-bands) compared to the monomeric species are attributed to the partially self-association of CR monomers in solution owing to strong intermolecular van der Waals-like attractive forces between the CR molecules[23].

This can occur because of a change in environmental conditions such as a change in solvent polarity will result in solvatochromism. Solvatochromism is the ability of a chemical substance to change color due to a change in solvent polarity. Negative solvatochromism corresponds to hypsochromic shift. Positive solvatochromism corresponds to bathochromic shift with increasing solvent polarity. The sign of the solvatochromism depends on the difference in dipole moment of the molecule of the dye between its ground state and excited state. For that reason, the heterogeneous Fenton-like oxidation conditions were conducted only within neutral and alkali pH range.

The pH of the wastewater is one of the vital parameter that determines the efficiency of heterogeneous Fenton–like process. Homogeneous Fenton process is efficient in pH range 2-4. However, heterogeneous Fenton type processes could be effectively operated at milder pH conditions. Thus, the experiments were conducted over a range of pH values from 7.5 to 12 at a fixed dye concentration (20 $mg.L^{-1}$), catalyst dosage (1 $g.L^{-1}$ of NZF) and H_2O_2 concentration (0.23 M).

As reported in fig. 10 and table 6, the degradation efficiency dramatically decreased from 92.07 to 31.60 % with parallel increase in pH from 7.5 to 10 and then it became constant beyond pH=10, almost reaching 32.89 % at pH=12. The optimum pH value was found to be 7.5 in which the reaction rate was the fastest and the maximum conversion (92.07%) was achieved within 60 min. To explain the relationship between the layer charge density and the sorption-desorption and subsequently the heterogeneous oxidation reactions, so-called Surface Complexation Model (SCM) was developed[25].

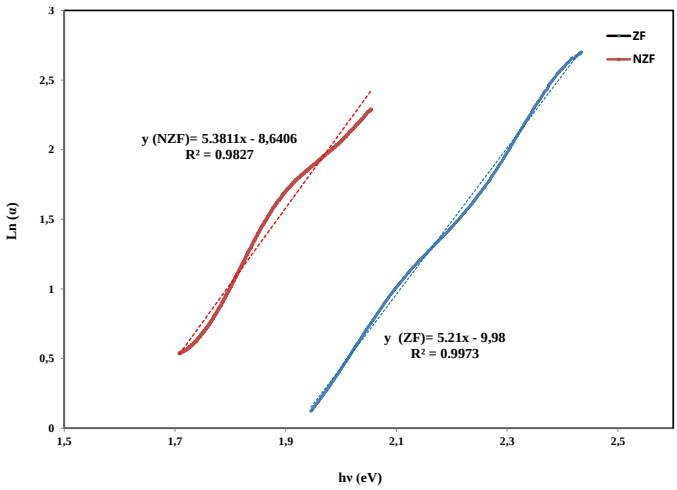

Fig. 7: Ln(α) versus hv ploting ZF and NZF nano-catalysts

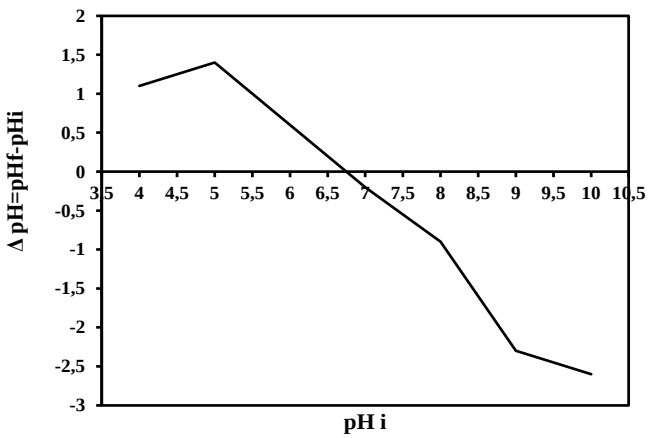

Fig. 8: The pH_{ZPC} of NZF nano-catalyst

In the 2-pK approach, we assume that most of the semiconductor oxides are amphoteric in nature, can associate or dissociate proton in aqueous solution. The pH_{ZPC} (the pH of zero point charge) of NZF nano-catalyst was 6.75. As a matter of fact, NZF nano-catalyst contains three surface species (Eq. 15):

$$\equiv Fe^{III}\text{-}H_3O^+,\ \equiv Fe^{III}\text{-}OH \text{ and } \equiv Fe^{III}\text{-}O^- \quad (15)$$

The catalyst surface has a net positive charge at pH < pH_{ZPC}, according to the following reaction (Eq. 16):

$$\equiv Fe^{III} + H_2O \rightarrow \equiv Fe^{III}\text{-}H_3O^+ \qquad pH < pH_{ZPC} \quad (16)$$

$Ni_{0.6}Zn_{0.4}Fe_2O_4$ surface becomes negatively charged for pH > pH_{ZPC} given by the following reaction (Eq. 17):

$$\equiv Fe^{III} + H_2O \rightarrow \equiv Fe^{III}\,O^- + OH^- \qquad pH > pH_{ZPC} \quad (17)$$

Congo red (CR) is an anionic azo dye that has two functional groups i.e. sulfonic acid group $-R-(SO_3)^-$ and amino group $-R-NH_2$. The pKa value of CR azo dye is 4. At lower pH values (pH≤4), CR displays J-bands (J aggregate) in its absorption spectrum. However, at higher pH values (pH> 4), CR molecule can be completely dissociated to the chlorite ions Na^+ and the sulfonic acid group $-R-(SO_3)^-$, thus becomes negative charged in water.

At pH =7.5, negatively charged groups $\equiv Fe^{III}\,O^-$ was available at the catalyst surface due to the presence of OH^- at the surface of NZF catalyst. These negatively charged groups are not able to adsorb the sulfonic acid species $-R-(SO_3)^-$ which show also negative charges, resulting in greater electrostatic repulsion (Eq. 18).

$$\equiv Fe^{III}\,O^- + {}^{2-}(SO_3)_2\text{–}R\text{–}(NH_3)_2 \rightarrow \equiv Fe^{III}\,O^- + {}^{2-}(SO_3)_2\text{–}R\text{–}(NH_3)_2 \quad (18)$$

Moreover, the adsorption of H_2O_2 species on the catalyst would decrease as the catalyst was covered with OH^-, thus affecting the reaction between catalytic species. However, these findings were in dissimilar tendency to the reported value of 51.81 % of CR removal in the presence of NZF as displayed in table 6.

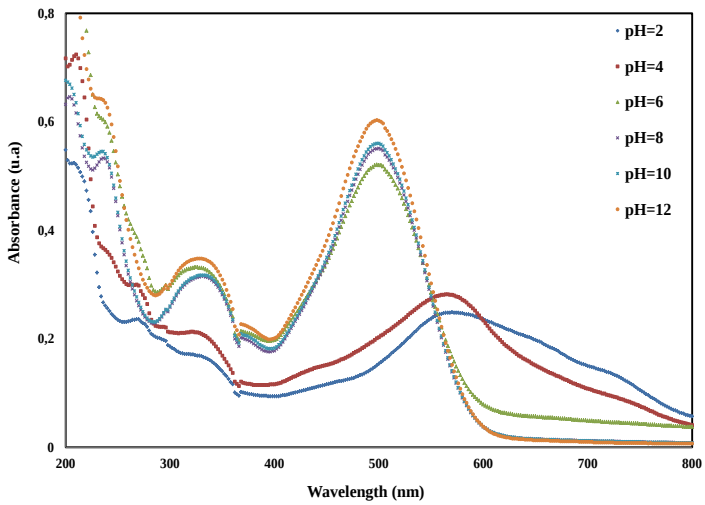

Fig. 9: Effect of pH on the UV-visible spectra of CR azo dye in aqueous solution

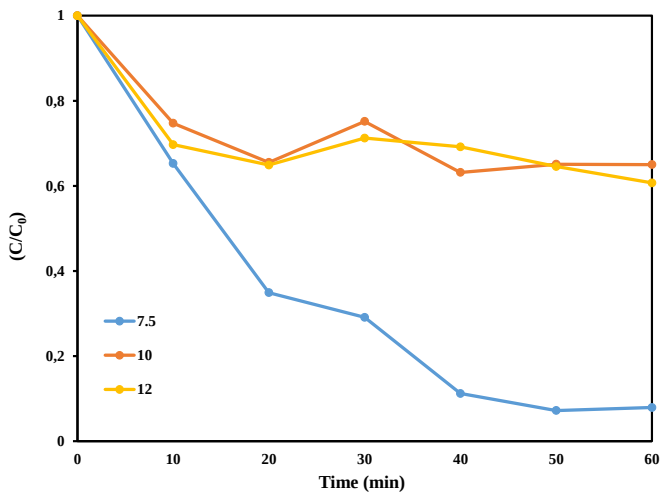

Fig. 10: Effect of pH solution on the heterogeneous oxidation of CR ([NZF]=1g.L^{-1}, [CR]=20 mg.L^{-1}, [H_2O_2]=0.23 M and, T=25 °C)

Based on the experimental results and a review of the literature[20,86], the heterogeneous Fenton-like catalytic mechanisms of NZF could be divided into two aspects:

1. The contribution of Na^+ ions in the adsorption process could not be ignored. Indeed, Na^+ can act as a cation bridge between the negatively charged $^{2-}(SO_3)_2$–R–$(NH_3)_2$ and the negative charges of the $\equiv Fe^{III}$ -O^-, possibly forming a complex [$\equiv Fe^{III}$ -O^- -- Na+ --$^{2-}(SO_3)_2$–R–$(NH_3)_2$], facilitating greater dye adsorption (Eq. 19).

$$\equiv Fe^{III}\text{-}O^- + Na^+ + {}^{2-}(SO_3)_2\text{–R–}(NH_3)_2 \rightarrow [\equiv Fe^{III}\text{-}O^- \text{ -- } Na^+ \text{ --}{}^{2-}(SO_3)_2\text{–R–}(NH_3)_2] \quad (19)$$

This can be confirmed by the role of cation-π bonding between the protonated amino group of oxytetracycline (OTC) and the graphene π electrons of multiwalled carbon nanotubes (MWCNTs) in the presence of $CaCl_2$[10]. They suggested that Ca^{2+} ions may simultaneously bind with the negatively charged OTC and interact either with the negative charges or the graphene π-electrons of the MWCNTs via cation-π bonding, leading to lower desorption (higher adsorption) of OTC.

2. The hydrogen peroxide may favor the more negatively charged oxide surface through establishment of strong complexes with compounds possessing weak base sites such as $\equiv Fe^{III}$ -O^-[84]. Initially, H_2O_2 was chemically absorbed on the surface of NZF catalyst and the NZF–H_2O_2 complex was then created as depicted in eq. 20. Moreover, the complexed Fe^{3+}/Fe^{2+} could decrease the Fe^{3+}/Fe^{2+} redox potential significantly. Therefore, the Fe^{3+}/Fe^{2+} cycle was greatly boosted and more reactive oxygen species such as $^{\bullet}OH$ and $O_2^{\bullet-}$ /$HO_2^{\bullet}$ were then produced via radical mechanism according to the Haber–Weiss mechanism (Eq. 21 to Eq. 23) which is primary responsible for the efficient degradation of CR at pH=7.5. Thus, the degradation efficiency of NZF towards the CR species increased greatly at pH=7.5.

$$\equiv Fe^{III} \text{ sites} + H_2O_2 \rightarrow \equiv Fe^{III} \text{ sites } H_2O_2 \quad (20)$$
$$\equiv Fe^{III} \text{ sites } H_2O_2 \rightarrow \equiv Fe^{II} \text{ sites} + HO_2^{\cdot} + H^+ \quad (21)$$
$$\equiv Fe^{III} \text{ sites} + HO_2^{\cdot} \rightarrow \equiv Fe^{II} \text{ sites} + O_2 + H^+ \quad (22)$$
$$\equiv Fe^{II} \text{ sites} + H_2O_2 \rightarrow \equiv Fe^{III} \text{ sites} + {}^{\cdot}OH + OH^- \quad (23)$$

However, the degradation efficiency was dramatically reduced to 31.60 and 32.89 % at pH =10 and 12, respectively. As pH was increased, both NZF surfaces and CR molecules became more negatively charged; consequently, interacting more strongly with Na^+ atom, leading to the adsorption. Despite adding H_2O_2 to dye solutions, the reduction of CR proceeded very slowly.

According to the previous discussed results, the main reasons for this underperformance could be as follows**:** (i) the availability of OH^-groups at alkaline pH and the adsorption of H_2O_2 on the catalyst would decrease as the catalyst was attached with the positively charged Na^+, thus affecting the reaction between catalytic species and H_2O_2 (Eq. 24). (ii) H_2O_2 is unstable at higher pH (alkaline solution) and its auto decomposition produces H_2O and O_2 molecules and lose its oxidation capability (Eq. 25). (iii) the activity of the Fenton reagent was reduced at higher pH values due to the sharp decrease of reaction rate which probably can be attributed to the formation of relatively inactive ferryl ions (FeO^{2+}) (Eq. 26) and (iv) a high-valent iron species ($Fe^{IV=0}$) might be generated in alkaline solutions, which is less reactive than hydroxyl radicals ($^{\cdot}OH$) (Eq. 27).

Hence, the activity of the heterogeneous Fenton reagent was reduced at higher pH values owing to the sharp decrease of reaction rate.

$$[\equiv Fe^{III}\, O^- \text{ -- } Na^+ \text{ -- } {}^{2-}(SO_3)_2\text{–R–}(NH_3)_2] + H_2O_2 \rightarrow [\equiv Fe^{III}\, O^- \text{ -- } Na^+ \text{ -- } {}^{2-}(SO_3)_2\text{–R–}(NH_3)_2] + H_2O_2 \quad (24)$$
$$2H_2O_2 \rightarrow O_2 + 2H_2O \quad (25)$$
$$\equiv Fe^{III}\, O^- + Na^+ \rightarrow \equiv Fe^{III}\, O^- + Na^+ \quad (26)$$
$$\equiv Fe^{II} + H_2O_2 \rightarrow \equiv Fe^{IV=0} + H_2O \quad (27)$$

As a result, the heterogeneous Fenton type processes could be effectively operated at milder pH conditions and the maximum 92.07 % degradation efficiency pH was obtained at pH 7.4 within 60 min. Based on our results, additional research will be carried out at a pH of 7.5.

The rate constant values, k_{app} (min^{-1}) and the half-life time $t_{1/2}$ were calculated from the slopes of the straight-line portion of the first-order plots ln (C/C_0) as a function of the exposure time at various pH solutions and the results are displayed in table 6.

The peroxide hydrogen is critical parameter for the degradation of the CR dye during Fenton oxidation. The impact of H_2O_2 concentration on the degradation of CR azo dye during Heterogeneous Fenton-like oxidation was investigated in the range of H_2O_2 concentration from 0.03 to 0.35 M at a fixed dye concentration of 20 mg/L, catalyst loading of 0.1 g/L, pH solution of 7.5 and 25 °C. The impact of H_2O_2 concentration on the degradation efficiency of NZF towards CR is depicted in fig. 11. Obviously, one can see from table 6 that the heterogeneous Fenton-like reaction is relatively sensitive to the H_2O_2 concentration.

It has been observed that degradation efficiency slowly increased from 54.67 to 59.09 % with the increase in the H_2O_2 concentration from 0.03 to 0.12 M at a reaction time of 60 min. However, the dye degradation efficiency was hastily raised beyond H_2O_2 concentration of 0.12 M achieving the efficiencies of 90.39 and 92.72 % at 0.17 and 0.23M of H_2O_2 respectively. Further increase in H_2O_2 concentration (i.e. 0.35 M), the degradation efficiency was dramatically reduced, almost reaching 57.54 %.

At low concentrations (i.e. H_2O_2 = 0.03-0.12 M), the decomposition of dissolved H_2O_2 on the catalyst surface of NZF was rather low, producing less hydroxyl radicals ($^{\bullet}OH$)

which reduced the rate of oxidation and slightly decreased the degradation efficiency[6].

However, with further H_2O_2 concentration increase beyond of 0.12 M, the degradation efficiency of NZF catalyst significantly declined, almost achieving 57.54 % at H_2O_2 concentration of 0.35 M. This phenomenon could be explained by the three possible reasons. First, the generation of hydroperoxyl radicals ($HO_2^{\cdot}$), which act as scavengers of hydroxyl radicals ($^{\bullet}OH$) (Eq. 28). Second, $^{\cdot}OH$ radicals exhibited much lower oxidation capabilities and did not contribute to the CR degradation (Eq. 29) which resulted in a decrease in the degradation efficiency. Third, the radical–radical reaction (Eq. 30) may occur in competition to radical–organic reactions, thus leading to the more consumption of $^{\bullet}OH$, which would not be consumed by the dye. Based on our obtained results, 0.23 M of H_2O_2 was used in subsequent experiments.

$$H_2O_2 + {}^{\bullet}OH \rightarrow H_2O + HO^{\bullet}_2 \quad (28)$$
$$HO^{\bullet}_2 + {}^{\bullet}OH \rightarrow H_2O + O_2 \quad (29)$$
$$^{\bullet}OH + {}^{\bullet}OH \rightarrow H_2O_2 \quad (30)$$

Kinetic data of the heterogeneous oxidation of CR azo dye at various H_2O_2 concentrations were analyzed using the pseudo-first-order kinetic model and the results are listed in table 6.

The purpose of the experiments was to investigate the effect of initial dye concentrations on degradation efficiency of ZNF/H_2O_2 catalytic system towards CR dye. The experiments were performed at H_2O_2 concentration of 0.23M, NZF catalyst dose of 1 g/L, pH 7.5, 25°C and various CR concentrations ranging from 10 to 50 mg/ L. As shown in fig. 12, the oxidation kinetic of the CR via the heterogeneous Fenton-like process (NZF/H_2O_2 system) decreased with time and then achieved equilibrium after 60 min. The degradation efficiency considerably rises from 52.46 to 92.07% as the initial CR concentration was increased from 10 to 20 mg/L and then noticeably decreased to 19.17 % for 50 mg/L. Optimum concentration of CR dye removal (up to ≈ 92.07%) was obtained at 20 mg/L.

At low initial concentration (i.e. 10 g/L), the rate of oxidation of CR (52.46 %) was slightly low owing to the self-scavenging effect of $^{\cdot}OH$ by excess Fe^{2+} in the NZF, subsequently the lifetime of $^{\cdot}OH$ radicals and the probability of collision between CR molecules and $^{\cdot}OH$ radicals were reduced[1]. Furthermore, an increase in CR concentration up to 20 mg.L^{-1}, the degradation efficiency of NZF catalyst obviously increases to 92.1%. For given catalyst dosage (m/v ration =0.23 M) and duration of oxidation (60 min), the available $^{\cdot}OH$ radicals on the catalyst surface are sufficient to immediately react with CR molecules and consequently result in an enhancement in the rate of oxidation of CR.

However, at higher amount of molecules (i.e. 30-50 mg/L) in the suspension, gradually CR molecules were adsorbed on the surface of the NZF catalyst which have an inhibitive effect on the reaction of CR molecules with $^{\cdot}OH$ radicals due to the lesser driving force of concentration gradient between CR and NZF catalyst and the deactivation of iron active sites of the catalyst, resulting in an inadequate production of $^{\bullet}OH$ radicals for the CR degradation. Besides, the free and available $^{\bullet}OH$ radicals compete with the active sites on the surface of NZF for the target CR molecules (Eq. 31 and Eq. 32). It is important to highlight that a lower oxidant H_2O_2/CR dye molar ratio was unfavorable in the NZF heterogeneous Fenton-like system, which may be due to the limited generation rate of $^{\bullet}OH$ radicals in the solution. Therefore, 20 g/L of CR was selected as the dye concentration for the following experiments.

$$\equiv Fe^{2+} + {}^{\bullet}OH \rightarrow \equiv Fe^{3+} + OH^{-} \quad (31)$$

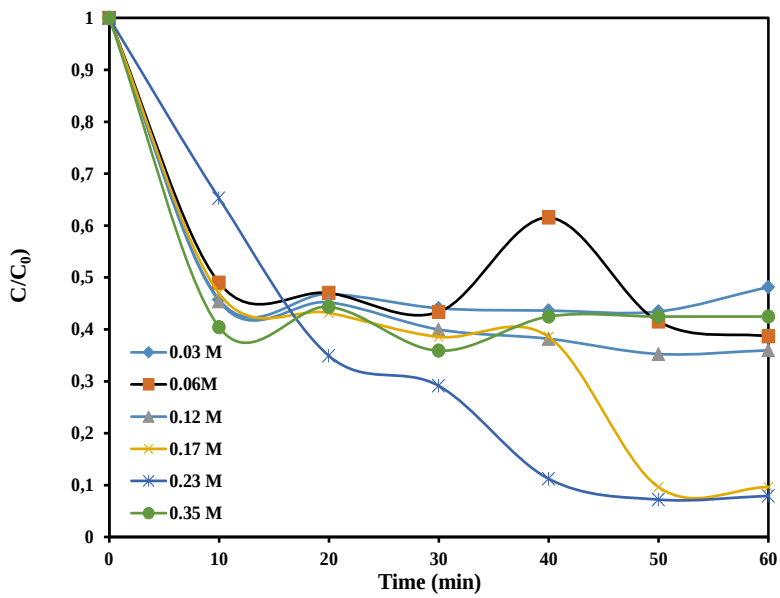

Fig. 11: Effect of H_2O_2 concentration on the heterogeneous oxidation of CR ([NZF]=0.1 g.L^{-1},[CR]=20 mg.L^{-1}, pH=7.5 and T=25 °C)

$$\equiv Fe^{2+} + {}^{\bullet}OOH \rightarrow \equiv Fe^{3+} + OOH^{-} \quad (32)$$

Fig. 13 depicts the time dependence of Ln (C/C_0) as a function of initial concentrations. The linear plots of Ln (C/C_0) vs. t, indicate a typical first-order reaction. The kinetics parameters: the rate constants K_{app} and the half-life time, $t_{1/2}$ were obtained from the linear regression (Table 6).

The effect of the catalyst dosage on the degradation of CR was studied by varying the catalyst dosage m/v from 0.25 to 1.5 $g.L^{-1}$ while keeping constant all the other operating parameters; initial CR concentration 20 $mg.L^{-1}$, H_2O_2 concentration of 0.23 M, pH 7.5 and 25°C. As shown in fig. 14, at low catalyst dosages (i.e. m/v = 0.50 $g.L^{-1}$), the degradation efficiency of 14.07 % was obtained in 60 min of exposure oxidation time. By increasing dosage of catalyst from 0.5 to 1.5 $g.L^{-1}$, the efficiency increased from 14.07 % (m/v=0.5 $g.L^{-1}$) to 92.07 % (m/v=1 $g.L^{-1}$) and thereafter decreases almost reaching 15.32% (m/v=1.5 g/L). Therefore, the degradation of CR was significantly affected by the dosage of catalyst. The optimum dosage was observed at 1 g/ L of catalyst and 92.07% degradation was achieved within 60 min.

An increase in catalyst dosage from 0.5 to 1g/L would lead to more production of the available iron active sites on the surface of the catalyst for activation of H_2O_2 to generate more free reactive hydroxyl radicals ($^{\bullet}OH$), thus enhancing the degradation efficiency of CR. However, when catalyst dosage further increased beyond 1 g/L, the degradation efficiency of CR was gradually decreased. The results can be attributed to increase in the rate of decomposition of H_2O_2 to O_2 owing to thermodynamic and mass transfer limitation.

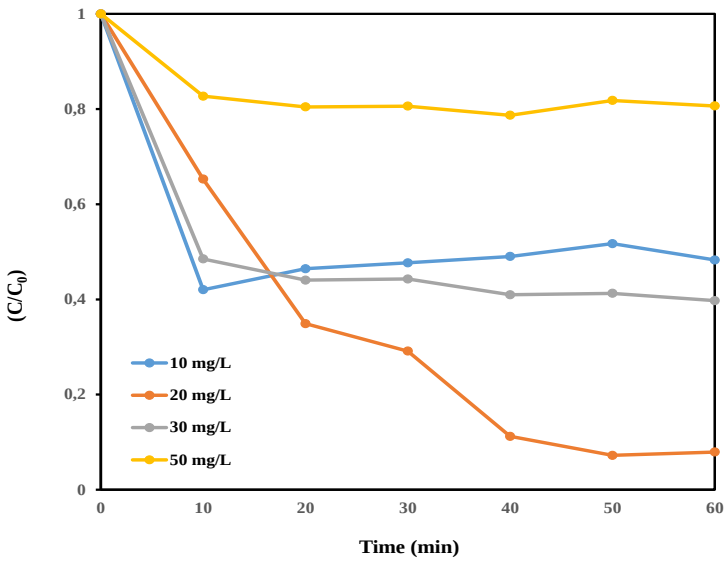

Fig. 12: Effect of initial CR concentration on the heterogeneous oxidation of CR ([NZF]=1 $g.L^{-1}$, [H_2O_2]=0.23M, pH=7.5 and T=25 °C)

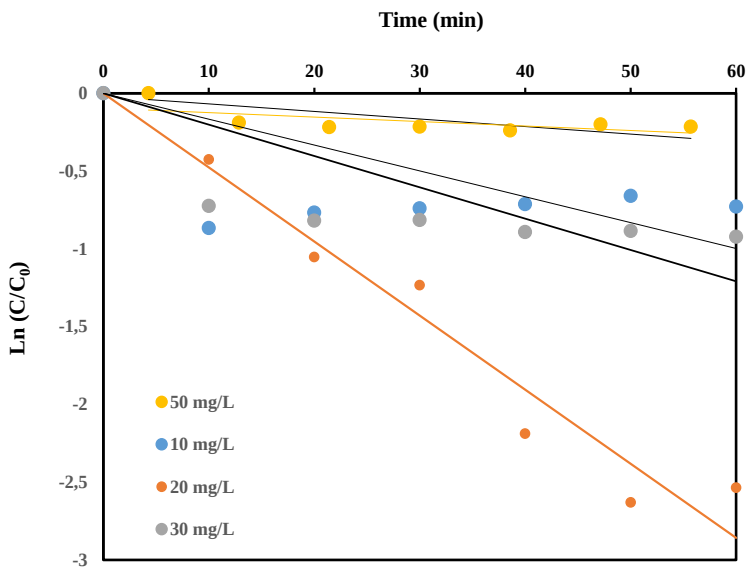

Fig. 13: Pseudo-first-order kinetics for heterogeneous oxidation of the CR at various initial CR concentrations ([NZF]=1 $g.L^{-1}$, [H_2O_2]=0.23M, pH=7.5 and T=25 °C)

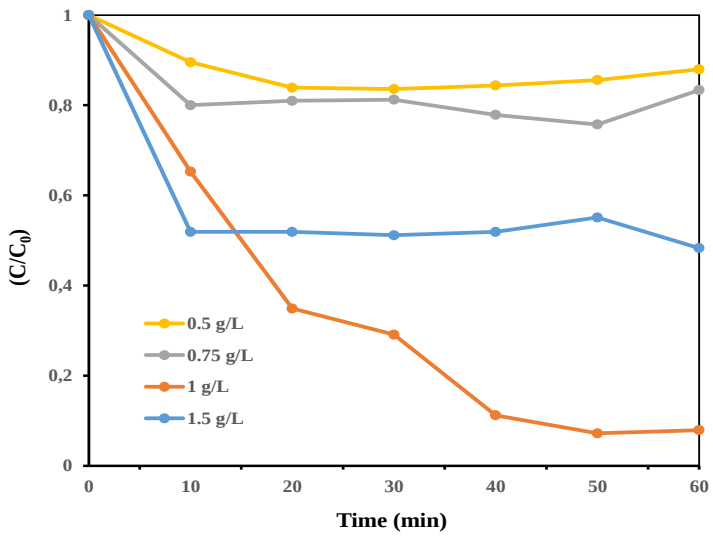

Fig. 14: Effect of NZF catalyst dosage on the heterogeneous oxidation of CR ([CR]=20 mg.L^{-1}, [H_2O_2]=0.23 M, pH=7.5 ,T=25 °C)

Moreover, the scavenging effect of ˙OH radicals by the excess Fe (II) ions on the surface of the catalyst (Eq. 33 and Eq. 34) and the tendency toward agglomeration of NZF NPs are probably the primary factors responsible for the reduction of the oxidation rate [5]. Thus, a nearly complete degradation was achieved at the optimum catalyst dosage of 1 g/L for 60 min of the heterogeneous Fenton like reaction. Thus, 1g/L of NZF was selected as the catalyst dosage for the subsequent experiments.

$$\equiv\text{FeII sites} + {}^{\cdot}\text{OH} \rightarrow \equiv\text{FeIII sites} + \text{OH}^- \quad (33)$$
$$\equiv\text{FeII sites} + {}^{\bullet}\text{OOH} \equiv\text{FeIII sites} + \text{OOH}^- \quad (34)$$

The kinetic data of the heterogeneous Fenton-like oxidation of CR using NZF as various doses were carried out under pseudo-first order model conditions. The plots of ln (C/C_0) versus time were drown as shown in the inset of fig. 15. The straight lines of these curves (until to 60 min) indicate that the heterogeneous oxidation at different CR dye concentration is pseudo-first order. The kinetic data from pseudo-first-order model Kinetics are tabulated in table 6.

To understand the effect of temperature, the heterogeneous oxidation studies were investigated by varying the temperatures from 25 to 60 °C at the optimum conditions: 20 mgL^{-1} of CR, 1g/L^{-1} NZF catalyst, 0.23 M of H_2O_2 and pH 7.5. Fig. 16 depicts the plot of heterogeneous oxidation of CR as a function of reaction time at various temperatures. It should be noted that that a higher temperature enhances the rate of formation of the ˙OH radicals according to the Arrhenius law, but also favors the decomposition of hydrogen peroxide into oxygen and water which reduces the efficiency of the heterogeneous Fenton process.

In addition, gradually increase in the temperature, the rate of diffusion of the adsorbate molecules across the external boundary layer and in the internal pores of the adsorbent particle were increased owing to the decrease in the viscosity of the solution[21].

Indeed, once the temperature was increased from 25 to 60 °C, the heterogeneous oxidation of CR by NZF/H_2O_2 process drastically declined from 92.07 to 29.45%. Three possible reasons explain this behavior. First, it could be attributed to the decreased oxygen solubility in water[64]. The second reason is the non-stability of H_2O_2 at high temperature more than 25°C (room temperature), which affects the degradation efficiency of the catalyst through its auto-decomposition to give H_2O and O_2 (Eq. 35).[62]

However, considering the degradation efficiency and thermal energy supply in the form of temperature heat, 25 °C was selected as optimal operating temperature for further experiments.

$$2H_2O_2 \rightarrow O_2 + 2H_2O \quad (35)$$

In this study, the pseudo-first order model was used to describe the heterogeneous Fenton-like process (NZF/H_2O_2 system) at various temperatures of system. The plot of ln (C/C_0) against time (t) is a straight line as illustrated in fig. 17. This suggests that the heterogeneous oxidation of CR dye at different temperature follows a pseudo first-order rate law. The data obtained for the kinetics experiment are shown in table 6.

The dissolved inorganic anions exist in water and in dye-containing industrial wastewater. These substances may compete for the active sites on the catalyst surface or deactivate the catalyst. Thus, the degradation rates of the target dye decrease. Hydroxyl radicals are non-selective and high reactive radicals with an oxidation potential which are relatively high as compared to common oxidizing agents like (H_2O_2, O_3, O_2 …). These ˙OH radicals react with non-target compounds present in the background water matrix such as dye auxiliaries present in the dye bath. They cause higher ˙OH radicals demand to achieve desired degree of degradation, or complete inhibition of advanced degradation rate and efficiency[2].

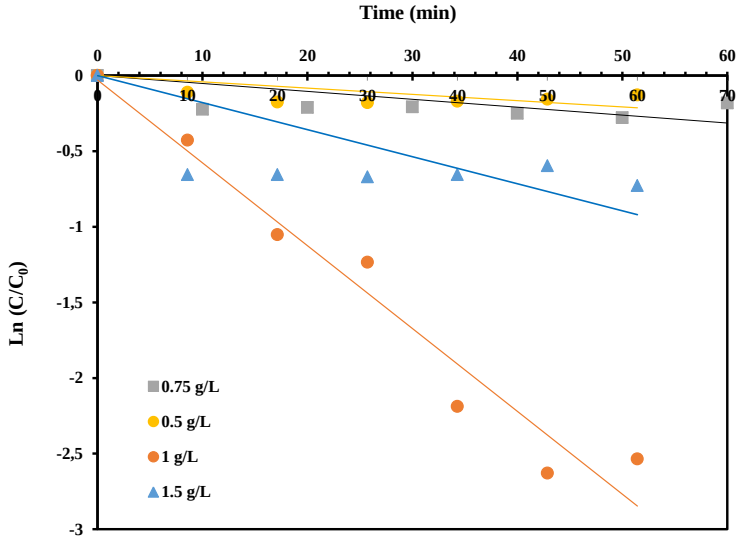

Fig. 15: Pseudo-first-order kinetics for heterogeneous oxidation of the CR at various catalyst dosage of NZF ([CR]=20 mg.L^{-1}, [H_2O_2]=0.23 M, pH=7.5 ,T=25 °C)

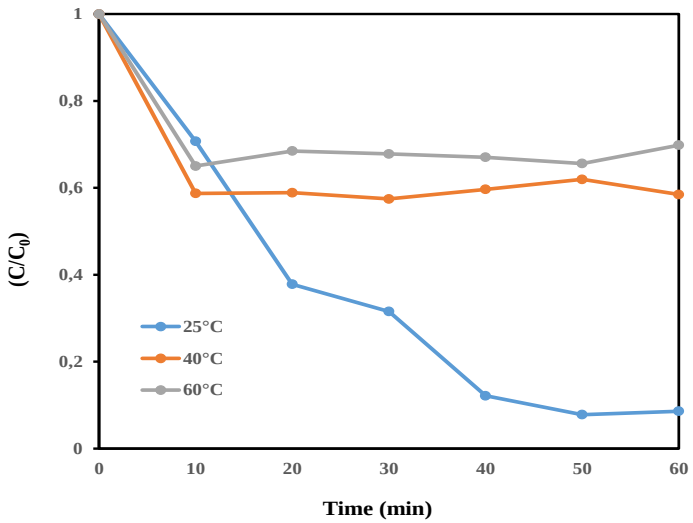

Fig. 16: Effect of temperature on the heterogeneous oxidation of CR temperature ([NZF]=1 g.L^{-1}, [CR]=20 mg.L^{-1}, [H_2O_2]=0.23 M and pH=7.5)

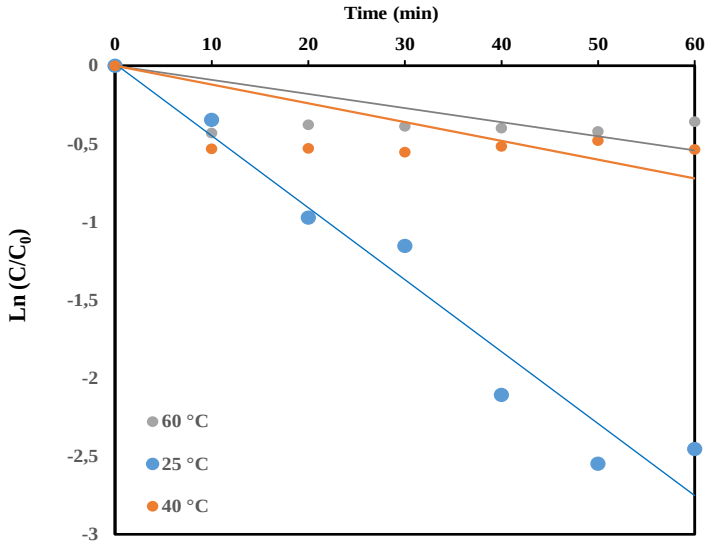

Fig. 17: Pseudo-first-order kinetics for heterogeneous oxidation of CR at various temperature ([NZF]=1 g.L^{-1}, [CR]=20 mg.L^{-1}, [H_2O_2]=0.23 M and pH=7.5)

Effect of the inorganic salt (i.e. Na_2CO_3) on the degradation of CR using NZF as a heterogeneous Fenton-like nano-catalyst was also investigated in the concentration range from 0 to 10 g.L^{-1}, while maintaining constant all the other operating parameters: 20 mg.L^{-1} of CR, 1g.L^{-1} of NZF catalyst, 0.23 M of H_2O_2, pH 7.5 and 25 °C. The experimental data are shown in fig. 18 and results are displayed in table 6.

Table 6
Rate constant and the half-life time values of degradation of CR by NZF catalyst as a function of different investigated parameters

Investigated parameters	Value	η'(%)	K x 10 (min^{-1})	$t_{1/2}$ (min)
pH of solution	7.5	92.07	3.8	49.15
	10	31.60	0.78	8.92
	12	32.89	0.81	8.56
H_2O_2 concentration (M)	0.03	54.67	1.52	4.560
	0.06	56.09	1.52	4.56
	0.12	59.94	1.84	3.77
	0.17	90.39	3.07	2.26
	0.23	92.07	3.8	49.15
	0.35	57.54	1.99	3.48
Dye concentration (mg. L^{-1})	10	52.46	1.4	49.5
	20	92.07	3.8	49.15
	30	56.86	1.67	41.5
	50	19.17	0.41	16.91
Catalyst dose (g.L^{-1})	O.25	15.32	-	-
	0.5	14.07	0.29	23.91
	0.75	20.13	0.43	16.12
	1	92.07	3.8	49.15
	1.5	15.32	1.54	4.50
Temperature of system (°C)	25	92.07	3.8	49.15
	40	40.82	1.00	51.34
	60	29.45	0.66	52.11
Inorganic salt (g.L^{-1})	0	92.07	3.8	49.15
	2.5	1.27	-	-
	5	3.6	-	-
	10	32.52	-	-
Operating conditions	ZF	2.5 (*)	-	-
	ZF/H_2O_2	5	-	-
	NZF	51.81(*)	1.52	4.56
	NZF/H_2O_2	92.07	3.8	49.15

*: adsorption

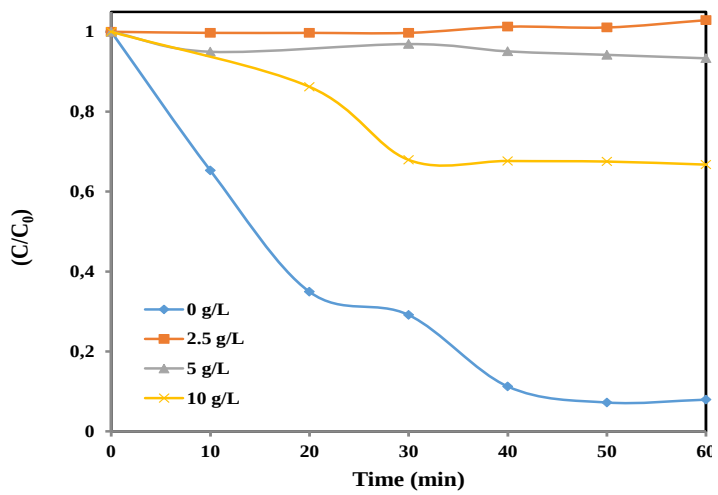

Fig. 18: Effect of Na_2CO_3 on the heterogeneous oxidation of CR ([NZF]=1 g.L^{-1}, [CR]=20 mg.L^{-1}, [H_2O_2]=0.23 M and pH=7.5 and T=25 °C)

Anionic species studied had inhibitory effect in the NZF/H_2O_2 system. The discrepancy in degradation efficiency observed for the whole Na_2CO_3 concentrations can be explained on the basis of two aspects. First, CO_3^{2-} anions compete with anionic form of CR dye for positively charged active sites at pH 7.5 available on the NZF surface (Eq. 36 and Eq. 37). Second, CO_3^{2-} anions react with $^{\bullet}OH$ radicals, through its scavenging effects, to form the corresponding radicals such as $CO_3^{\bullet-}$ (Eq. 38).

$$\equiv Fe^{III}\text{-}H_3O^+ + {}^-(SO_3)_2\text{–}R\text{–}(NH_2)_2 \rightarrow [\equiv Fe^{III}\text{-}H_3O\text{---}(SO_3)_2R\text{–}(NH_2)_2] \quad (36)$$

$$\equiv Fe^{III}\text{-}H_3O^+ + CO_3^{2-} \rightarrow [\equiv Fe^{III}\text{-}H_3O\text{-----}CO_3] \quad (37)$$

$$^{\bullet}OH + CO_3^{\bullet-} \rightarrow OH^- + CO_3^{\bullet-} \quad (38)$$

Although, the reactivity of the produced $CO_3^{\bullet-}$ anionic radicals may be considered, they are less reactive than OH due to their lower oxidation potentials[88].

The degradation efficiencies of NZF catalyst toward CR in various conditions such as NZF catalyst only (adsorption system) and NZF/H_2O_2 catalyst system (heterogeneous Fenton-like process employing iron-based catalyst) compared with that of the pristine ZF were investigated. As shown in table 6, up to ≈54% of CR was degraded after 60 min with NZF catalyst only. However, the mixture of magnetic NZF and H_2O_2 leads to a high degradation rate (up to ≈92 %) which was attributed to synergetic effect of iron-based catalyst, which resulted in increased production of hydroxyl radicals and direct oxidation of CR species indicating that NZF is a heterogeneous Fenton-like catalyst[46].

Conclusion

In this study, $ZnFe_2O_4$ (ZF) and $Ni_{0.6}Zn_{0.4}Fe_2O_4$ (NZF) stable magnetically nano-ferrospinel particles were successfully synthesized by a facile sol-gel method for heterogeneous Fenton-like oxidation of azo dye (i.e. Congo red) from the industrial aqueous media. The prepared materials were characterized by XRD, SEM and UV-vis-DRS. Single phase product formation was confirmed by XRD and SEM. From XRD and UV-vis-DRS results, it is highlighted that average crystallite size and band gap energy are decreased owing to nickel ion substitution.

NZF exhibited high catalytic efficiency (up to ~92%) to reduce CR within 60 min under optimum conditions of 20 mg L^{-1} CR, 0.23 M H_2O_2, 1 g L^{-1} catalyst, pH = 7.5 and 25 °C. The heterogeneous Fenton-like oxidations Kinetics were correlated with pseudo first-order reaction. A plausible mechanism of the increased heterogeneous Fenton-like activity in NZF/H_2O_2 process was proposed.

Acknowledgement

The authors would like to thank the University of Sciences and Technology of Oran Mohamed Boudiaf (U.S.T.O.M.B.) and the University of Saida for providing materials support to this research.

References

1. Ajoudanian N. and Nezamzadeh-Ejhieh A., Enhanced photocatalytic activity of nickel oxide supported on clinoptilolite nanoparticles for the photodegradation of aqueous cephalexin, *Mat. Sci. Semicond. Processing*., **36**, 162 **(2015)**

2. Alahiane S., Qourzal S., El Ouardi M., Belmouden M., Assabbane A. and Ait-Ichou Y., Adsorption and photocatalytic degradation of indigo carmine dye in aqueous solutions using TiO_2/UV/O_2), *J. Mater. Environ. Sci.*, **4**, 239 **(2013)**

3. Armendariz H., Aguilar G., Salas P., Valenzuela M.A., Schifter I., Arriola H. and Nava N., Oxidative dehydrogenation of n-butane on iron-zinc oxide catalysts, *Appl. Catal. A*., **92**, 29 **(1992)**

4. Azàroff L.V., Elements of X-Ray Crystallography, McGraw-Hill, New-York **(1968)**

5. Azimia S. and Nezamzadeh-Ejhieha A., Enhanced activity of clinoptilolite-supported hybridized PbS–CdS semiconductors for the photocatalytic degradation of a mixture of tetracycline and cephalexin aqueous solution, *J. Molecular Cat. A. Chem*., **408**, 152 **(2015)**

6. Benhadria N., Elaziouti A., Laouedj N., Sellami M. and Bettahar N., Synthesis and characterization of $Bi_{1.56}Sb_{1.48}Co_{0.96}O_7$ pyrochlore sun-light-responsive photocatalyst, *Mater. Resear Bull*., **74**, 491 **(2016)**

7. Bhattacharya D., Chaudhuri S. and Pal A.K., Bandgap and optical transitions in thin films from reflectance measurements, *Vacuum*., **43**, 313 **(1992)**

8. Boreddy R., Materials and Production Engineering, University "Federico II" of Naples, Italy **(2011)**

9. Boudjemaa A., Popescu I., Juzsakovac T., Kebir M., Helaili N., Bachari K. and Marcu I.C., M-substituted (M = Co, Ni and Cu) zinc ferrite photo-catalysts for hydrogen production by water photo-reduction, *Inter. J. Hydrogen Energy*, **41**,11108 **(2016)**

10. Bui T.X. and Choi H., Comment on "Adsorption and desorption of oxytetracycline and carbamazepine by multiwalled carbon nanotubes", *Environ. Sci. Technol*., **44**, 4828 **(2010)**

11. Cao X., Gu L., Lan X., Zhao C., Yao D. and Sheng W., Spinel $ZnFe_2O_4$ nanoplates embedded D. with Ag clusters: Preparation, characterization and photocatalytic application, *Mater. Chem. Phys*., **106**, 175 **(2007)**

12. Chae W.S., Ko J.H., Choi K.H., Jung J.S. and Kim Y.R., *J. Anal. Sc. Technol*., **1**, 25 **(2010)**

13. Chen C.H., Liang Y.H. and Zhang W.D., $ZnFe_2O_4$/MWCNTs composite with enhanced photocatalytic activity under visible-light irradiation, *J. Alloys Comp.*, **501**, 168 **(2010)**

14. Chen J.L., Chen D., He J.J., Zhang S.Y. and Chen Z.H., The microstructure, optical and electrical properties of sol–gel-derived Sc-doped and Al–Sc co-doped ZnO thin films, *Appl. Surf. Sci*., **255**, 9413 **(2009)**

15. Cheng P., Deng C.S., Gu M.Y. and Shangguan W.F., Visible-light responsive zinc ferrite doped titania photocatalyst for methyl orange degradation, *J. Mater. Sci.*, **42**, 9239 **(2007)**

16. Cheng P., Li W., Zhou T.L., Jin Y.P. and Gu M.Y., Physical and photocatalytic properties of zinc ferrite doped titania under visible light irradiation, *J. Photochem. Photobiol.*, A., **168**, 97 **(2004)**

17. Chinnasamy C.N., Narayanasamy A., Ponpandian N., Chattopadhyay K., Guerault H. and Greneche J.M., Magnetic properties of nanostructured ferrimagnetic zinc ferrite, *J. Phys. Condens. Matter*., **12**, 7795 **(2000)**

18. Choi Y., Shim H.S. and Lee J.S., Study on magnetic properties and structural analysis of Ni–Zn ferrite prepared through self-propagating high-temperature synthesis reaction by neutron diffractometry, *J. Alloys. Compd*., **326**, 56 **(2001)**

19. Chou S. and Huang C., Application of a supported iron oxyhydroxide catalyst in oxidation of benzoic acid by hydeogen peroxide, *Chemosphere*, **38**, 2719 **(1999)**

20. Chou S. and Huang C., Decomposition of hydrogen peroxide in a catalytic fluidized-bed reactor, *Applied Catalysis A: General*, **185**, 237 **(1999)**

21. Dogan M., Alkan M., Turkyilmaz A. and Ozdemir Y., Kinetics and mechanism of removal of methylene blue by adsorption onto perlite, *J. Hazard Mater*., **109**, 141 **(2004)**

22. Elaziouti A., Laouedj N. and Bekka A., Preparation and characterization of novel $CuBi_2O_4$ /SnO_2 p–n heterojunction with enhanced photocatalytic performance under UVA light irradiation, *J. King. Saud. Uni.*, **27**, 76 **(2015)**

23. Elaziouti A., Laouedj N. and Bekka A., Synthesis, characterization and UV-A light photocatalytic activity of 20wt%SrO–$CuBi_2O_4$ composite, *Applied Surface Science*, **258**, 5010 **(2012)**

24. Elaziouti A., Laouedj N., Benhadria N. and Bettahar N., SnO_2 foam grain-shaped nanoparticles: Synthesis, characterization and UVA light induced photocatalysis, *J. Alloys Compd*., **679**, 408 **(2016)**

25. Fernandez J., Kiwi J., Lizama C., Freer J., Baeza J. and Mansilla H.D., Factorial experimental design of Orange II photocatalytic discolouration, *J. Photochem. Photobiol. A: Chem.*, **151**, 213 **(2002)**

26. Frame F.A., Carroll E.C., Larsen D.S., Sarahan M., Browningb N.D. and Osterloh F.E., First demonstration of CdSe as a photocatalyst for hydrogen evolution from water under UV *and* visible light, *Chem. Commun*., **2008**, 2206 **(2008)**

27. Frei E.H., Gunders E., Pajewsky M., Alkan W.J. and Eshchar J., Ferrites as contrast material for medical X-ray diagnosis, *J. Appl. Phys*., **39**, 999 **(1968)**

28. Fumiaki A., Eri I. and Akira Y., Effect of Particle Size on the Photocatalytic Activity of WO_3 Particles for Water Oxidation, *J. Phys. Chem. C.*, **117**, 22584 **(2013)**

29. Gao D.Q., Shi Z.H., Xu Y., Zhang J., Yang G.J., Zhang J.L., Wang X.H. and Xue D.S., Synthesis, Magnetic Anisotropy and Optical Properties of Preferred Oriented Zinc Ferrite Nanowire Arrays, *Nanoscale Res. Lett*., **5**, 1289 **(2010)**

30. Gar´cia-Jimeno S., Ortega-Palacios R., Cepeda-Rubio M.F.J., Vera A., Leija L. and Estelrich J., Improved thermal ablation efficacy using magnetic nanoparticles: a *study* in tumor phantoms, *Progress in Electrom Research*, **128**, 229 **(2012)**

31. Gubin S.P., Koksharov Y.A., Khomutov G.B. and Yurkov G.Y., Magnetic nanoparticles: preparation, structure and properties, *Russian Chem. Rev.*, **74**, 489 **(2005)**

32. Gul M. and Akhtar K., Synthesis of magnetic $ZnFe_{1.5}Al_{0.5}O_4$ nanoparticles and their photocatalytic activity testing under sunlight irradiation, *J. Sci. Innov. Res*., **6**, 19 **(2017)**

33. Han C., Lizhong Z., Hehua Z., Dongju Y., Qian Z., Xiufeng Z. and Jianhui L., Highly active iron-containing silicotungstate catalyst for heterogeneous Fenton oxidation of 4-chlorophenol, *J. Molec. Cat. A: Chemical*, **406**, 72 **(2015)**

34. Harish K. and Bhojya Naik H., Solar light active $ZnFe_{2-x}Al_xO_4$ materials for optical and photocatalytic activity: an efficient photocatalyst, *Inter. J. Sci. Res*., **4**, 301 **(2013)**

35. Hassanien A.S. and Ak A.A., Influence of composition on optical and dispersion parameters of thermally evaporated non-crystalline $Cd_{50}S_{50-x}Se_x$ thin films, *J. Alloys. Compd*., **648**, 280 **(2015)**

36. He H.Y., Huang J.F. and Lu J., Photo- and Photo-Fenton-like Catalytic Degradations of Malachite Green in a Water Using Magnetically Separable $ZnFe_2O_4$-reduced Graphene Oxide Hybrid Nanostructures, *J. Sci. Research & Reports*., **10**, 1 **(2016)**

37. Hu C., Zhang Z., Liu H., Gao P. and Lin Wang Z., Direct synthesis and structure characterization of ultrafine CeO_2 nanoparticles, *Nanotechnol.*, **17**, 5983 **(2006)**

38. Ibarguen C.A., Mosquera A., Parra R., Castro M.S. and Rodriguez-Paez J.E., Synthesis of SnO_2 nanoparticles through the controlled precipitation route, *Mater. Chem. Phys*., **101**, 433 **(2007)**

39. Jia Z., Ren D., Liang Y. and Zhu R., A new strategy for the preparation of porous zinc ferrite nanorods with subsequently light-driven photocatalytic activity, *Mat. Letters*, **65**, 3116 **(2011)**

40. Jin Y.X., Li G.H. and Zhang L.D., Pseudo-half-metallicity in the double perovskite Sr_2CrReO_6 from density-functional calculations, *Appl. Phys. Lett*., **86**, 032513 **(2005)**

41. Kaneva N.V. and Dushkin C.D., Tuning of the UV photocatalytic activity of ZnO using zinc ferrite(III): Powders and thin films prepared of powders, *Colloids Surf. A: Physicochem. Eng. Aspects*, **382**, 211 **(2011)**

42. Karunakaran C., Dhanalakshmi R. and Gomathisankar P., Photomineralization of phenol on Al_2O_3: synergistic photocatalysis by semiconductors, *Res. Chem. Intermed*., **36**, 361 **(2010)**

43. Bhawana J. et al, Treatment of organic pollutants by homogeneous and heterogeneous Fenton reaction processes, *Environmental Chemistry Letters*, **16**, 947 **(2018)**

44. Karunakaran C., Panneerselvam S.M. and Gomathisankar P., Photoreduction of chromium (VI) on ZrO_2 and ZnS surfaces, *Monatsh.Chem.*, **140**, 1269 **(2009)**

45. Kovalenko M.V., Bodnarchuk M.I., Stroyuk A.L. and Kuchmii S.Y., Spectral, optical and photocatalytic characteristics of quantum sized particles of CdTe, *Theo. Exp. Chem.*, **40**, 220 **(2004)**

46. Xu. L. and Wang J., Magnetic Nanoscaled Fe_3O_4/CeO_2 Composite as an Efficient Fenton-Like Heterogeneous Catalyst for Degradation of 4-Chlorophenol, *Environ. Sci. Technol*., **46**, 10145 **(2012)**

47. Landi G.T., Simple models for the heating curve in magnetic hyperthermia experiments, *J. Magnetism and Magnetic Mat*., **326**, 14 **(2013)**

48. Lee K.T. and Lu S.Y., A cost-effective, stable, magnetically recyclable photocatalyst of ultra-high organic pollutant degradation efficiency: $SnFe_2O_4$ nanocrystals from a carrier solvent assisted interfacial reaction process, *J. Mater. Chem.* A., **3**, 12259 **(2015)**

49. Lee K.T., Chuah X.F., Cheng Y.C. and Lu S.Y., Pt coupled $ZnFe_2O_4$ nanocrystals as a breakthrough photocatalyst for Fenton-like processes photodegradation treatments from hours to seconds, *J. Mater. Chem. A.*, **3**, 18578 **(2015)**

50. Li X.Y., Hou Y., Zhao Q.D., Teng W., Hu X.J. and Chen G.H., Capability of novel $ZnFe_2O_4$ nanotube arrays for visible-light induced degradation of 4-chlorophenol, *Chemosphere*, **82**, 581 **(2011)**

51. Lu H.C., Chang J.E., Vong W.W., Chen H.T. and Chen Y.L., Porous ferrite synthesis and catalytic effect on benzene degradation, *Inter. J. Phys. Sci*., **6**, 855 **(2011)**

52. Majeed M.I. et al, Highly water-soluble magnetic iron oxide (Fe_3O_4) nanoparticles for drug delivery: enhanced in vitro therapeutic efficacy of doxorubicin and MION conjugates, *J. Mat. Chem. B.*, **1**, 2874 **(2013)**

53. Manikandan A., Arul Antony S., Sridhar R., Ramakrishna S. and Bououdina M., A Simple Combustion Synthesis and Optical Studies of Magnetic $Zn_{1-x}NixFe_2O_4$ Nanostructures for Photoelectrochemical Applications, *J. Nanosc. Nanotechnol.*, **15**, 4948 **(2015)**

54. Manikandan A., Durka M. and Arul Antony S., A novel synthesis, structural, morphological and opto-magnetic characterizations of magnetically separable spinel CoxMn1-xFe_2O_4 ($0 \leq x \leq 1$) nano-catalysts, *J. Supercond. Nov. Magn.*, **27**, 2841 **(2014)**

55. Mary Jacintha A., Manikandan A., Chinnaraj K., Arul Antony S. and Neeraja P., Comparative studies of spinel $MnFe_2O_4$ nanostructures: Structural, morphological, optical, magnetic and catalytic properties, *J. Nanosci. Nanotechnol*., **15**, 9732 **(2015)**

56. Matsumoto Y., Energy Positions of Oxide Semiconductors and Photocatalysis with Iron Complex Oxides, *J. Solid.State.Chem.*, **126**, 227 **(1996)**

57. Mohamed Ali A., Kasim El-Sayed R., El-Shokrofy K.M., Abo Arais A. and Shams M.S., The Influence of Zn²⁺ Ions Substitution on the Microstructure and Transport Properties of Mn-Zn Nanoferrites, *Mat. Sci. Applications*, **5**, 932 **(2014)**

58. Mora-Sero I., Bisquert J., Dittrich T., Belaidi A., Susha A.S. and Rogach A.L., Photosensitization of TiO_2 Layers with CdSe Quantum Dots: Correlation between Light Absorption and Photoinjection, *J. Phys. Chem. C.*, **111**, 14889 (**2007**)

59. Muruganandha M., Suri R.P.S., Jerry J., Balachandran S. and Swaminathan M., Recent Developments in Heterogeneous Catalyzed Environmental Remediation Processes, *J. Nanosci. Nanotechnol.*, **14**, 1898 **(2014)**

60. Nalbandian L., Delimitis A., Zaspalis V.T., Deliyanni E.A., Bakoyannakis D.N. and Peleka E.N., Hydrothermally prepared nanocrystalline Mn–Zn ferrites: Synthesis and characterization, *Microporous and Mesoporous Materials*, **114**, 465 **(2008)**

61. Nazarkovsky M.A., Gun'ko V.M., Wójcik G., Czech B., Sobieszek A., Skubiszewska-Zieba J., Janusz W. and Skwarek E., Band-gap change and photocatalytic activity of silica/titania composite associated with incorporation of CuO and NiO, *Phys. Technol. Surf.*, **5**, 421 **(2014)**

62. Neamtu M., Catrinescu C. and Kettrup A., Effect of dealumination of iron(III) exchanged Y zeolites on oxidation of Reactive Yellow 84 azo dye in the presence of hydrogen peroxide, *Appl. Catal. B. Environ.*, **51**, 149 **(2004)**

63. Padmapriya G., Manikandan A., Krishnasamy V., Jaganathan S. K. and Antony S.A., Spinel $Ni_xZn_{1-x}Fe_2O_4$ ($0.0 \leq x \leq 1.0$) nano-photocatalysts: Synthesis, characterization and photocatalytic degradation of methylene blue dye, *J. Mol. Str*., **1119**, 39 **(2016)**

64. Pare B., Singh P. and Jonnalagadda S.B., Visible light-driven photocatalytic degradation and mineralization of neutral red dye in a slurry photoreactor, *Indian J. Chem. Technol*., **17**, 391 **(2010)**

65. Pariente M.I., Martínez F., Botas J.Á. and Melero J.A., Extrusion of Fe_2O_3/SBA-15 mesoporous material for application as heterogeneous Fenton-like catalyst, *AIMS Environ. Sci.*, **2**, 154 **(2015)**

66. Parkhomchuk E.V., Savinov E.N., Vostrikova L.A. and Parmon V.N., Heterogeneous catalysis in the Fenton-type system FeZSM-5/H_2O_2, *Appl. Cat. B Environmental.*, **51**, 165 **(2004)**

67. Phanichphant S., Nakaruk A. and Channei D., Photocatalytic activity of the binary composite CeO_2/SiO_2 for degradation of dye, *Appl. Surf. Sci*., **387**, 214 **(2016)**

68. Rache M.L., Garcia A.R., Zea H.R., Silva A.M.T., Madeira L.M. and Ramirez J.H., Azo-dye orange II degradation by the heterogeneous Fenton-like process using a zeolite Y-Fe catalyst—Kinetics with a model based on the Fermi's equation, *Appl. Catal. B: Environ.*, **146**, 192 **(2014)**

69. Rashad M.M. and Fouad O.A., Synthesis and characterization of nano-sized nickel ferrites from fly ash for catalytic oxidation of CO, *Mat.Chem. Phys*., **94**, 365 **(2005)**

70. Safari A., Gheisari Kh. and Farbod M., Investigation of structure and magneticproperties of NI ferrite powders synthesized by plasma arc discharge, *J. New Mat.*, **7**, 17 **(2017)**

71. Safari A., Gheisari Kh. and Farbod M., Characterization of Ni ferrites powders prepared by plasma arc discharge process, *J. Magnetism Magnetic Mat.*, **421**, 44 **(2017)**

72. Sangami G. and Dharmaraj N., UV–visible spectroscopic estimation of photodegradation of rhodamine- B dye using tin (IV) oxide nanoparticles, *Spectr. Chim. Acta Part A: Mol. Biomol. Spect*., **97**, 847 **(2012)**

73. Santos O.D., Weiler M.L., Junior D.Q. and Medina A.N., CO gas-sensing characteristics of SnO_2 ceramics obtained by chemical precipitation and freeze-drying, *Sens. Act. B*., **75**, 83 **(2001)**

74. Saravanan R., Gupta V.K., Mosquera E., Gracia F., Khan M.M., Narayanan V. and Stephen A., $ZnO/Ag/Mn_2O_3$ nanocomposite for visible light-induced industrial textile effluent degradation, uric acid and ascorbic acid sensing and antimicrobial activity, *RSC. Adv*., **5**, 34645 **(2015)**

75. Satyanarayana L., Reddy K.M. and Manorama S.V., Nanosized spinel $NiFe_2O_4$: A novel material for the detection of liquefied petroleum gas in air, *Mat. Chem. Phys*., **82**, 21 **(2003)**

76. Seiji K. and Toshiyuki A., Photocatalysis for water oxidation by Fe_2O_3 nanoparticles embedded in clay compound: correlation between its polymorphs and their photocatalytic activities, *J. Mater. Sci*., **44**, 2890 **(2009)**

77. Singh J.P., Srivastava R.C. and Agrawal H.M., Optical behaviour of zinc ferrite nanoparticles, AIP Conf. Proc., **1276**, 137 **(2010)**

78. Tauc J., Grigorovici R. and Vancu A., Optical properties and electronic structure of amorphous germanium, *Physica. Status. Solidi B*., **15**, 627 **(1966)**

79. Urbach F., The Long-Wavelength Edge of Photographic Sensitivity and of the Electronic Absorption of Solids, *Phys. Rev*., **92**, 1324 **(1953)**

80. Toledo J.A., Valenzuela M.A., Bosch P., Armendariz H., Montoya A., Nava N. and Vázquez A., Effect of Al^{3+} introduction into hydrothermally prepared $ZnFe_2O_4$, *Appl. Cat. A: General*, **198**, 235 **(2000)**

81. Valenzuela M.A., Bosch P., Jiménez-Becerrill J., Quiroz O. and Páez A.I., Preparation, characterization and photocatalytic activity of ZnO, Fe_2O_3 and $ZnFe_2O_4$, *J. Photochem. Photobiol.*, A., **148**, 177 **(2002)**

82. Verma A., Thakur O.P., Prakash C., Goel T.C. and Mendiratta R.G., Temperature dependence of electrical properties of nickel–zinc ferrites processed by the citrate precursor technique, *Mater. Sci. Eng. B*., **116**, 1 **(2005)**

83. Vora J.J., Chauhan S.K., Parmar K.C., Vasava S.B., Sharma S. and Bhutadiya L.S., Kinetic study of application of ZnO as a photocatalyst in heterogeneous medium, *E-J Chem*., **6**, 531 **(2009)**

84. Wallace J.G., Hydrogen Peroxide in Organic Chemistry, E.I. du Pont de Nemours & Co., Wilmington, Delaware **(1975)**

85. Wang H.W. and Kung S.C., Crystallization of nanosized Ni–Zn ferrite powders prepared by hydrothermal method, *J. Magn. Magn. Mater*., **270**, 230 **(2004)**

86. Wu J., Pu W., Yang C., Zhang M. and Zhang J., Removal of benzotriazole by heterogeneous photoelectro-Fenton like process using $ZnFe_2O_4$ nanoparticles as catalyst, *J. Environ. Sci*., **25**, 801 **(2013)**

87. Xie J.S., Wu Q.S. and Zhao D.F., Electrospinning synthesis of $ZnFe_2O_4/Fe_3O_4/Ag$ nanoparticle-loaded mesoporous carbon fibers with magnetic and photocatalytic properties, *Carbon*, **50**, 800 **(2012)**

88. Xie X., Zhang Y., Huang W. and Huang Sh., Degradation kinetics and mechanism of aniline by heat-assisted persulfate oxidation, *J. Environ. Sci*. **24**, 821 **(2012)**

89. Xu L. and Wang J., Magnetic Nanoscaled Fe_3O_4/CeO_2 Composite as an Efficient Fenton-Like Heterogeneous Catalyst for Degradation of 4-Chlorophenol, *Environ. Sci. Technol*., **46**, 10145 **(2012)**

90. Xu Y. and Schoonen M.A.A., The absolute energy positions of conduction and valence bands of selected semiconducting minerals, *Am. Mineral*., **85**, 543 **(2000)**

91. Yao Y., Qin J., Cai Y., Wei F., Lu F. and Wang S., Facile synthesis of magnetic $ZnFe_2O_4$–reduced graphene oxide hybrid and its photo-Fenton-like behavior under visible iradiation, *Environ. Sci. Pollut. Res.*, **21**, 7296 **(2014)**

92. Yunus A., Zahira aakob Y. and Parul Khtara A., Degradation and mineralization of methylene blue using a heterogeneous photo-Fenton catalyst under visible and solar light irradiation, *Catal. Sci. Technol.*, **6**, 1222 **(2016)**

93. Zahi S., Hashim M. and Daud A.R., Synthesis, magnetic properties and microstructure of Ni–Zn ferrite by sol–gel technique, *J. Magn. Magn. Mater*., **308**, 177 **(2007)**

94. Zhan J.L., Ghafar A., Kim H.J., Seong H.Y. and Sung O.C., $LiFePO_4$ microcrystals as an efficient heterogeneous Fenton-like catalyst in degradation of rhodamine 6G, *Nano Scale Res. Lett*., **9**, 276 **(2014)**

95. Zhang C. and Zhu Y.F., Synthesis of Square Bi_2WO_6 Nanoplates as High-Activity Visible-Light-Driven Photocatalysts, *Chem. Mater*., **17**, 3537 **(2005)**

96. Zhang L., He Y., Ye P., Wua Y. and Wua T., Visible light photocatalytic activities of $ZnFe_2O_4$ loaded by Ag_3VO_4 heterojunction composites, *J. Alloys Compd*., **549**, 105 **(2013)**

97. Zhong C., Xueqiang C., Lixian S. and Yinghe H., Photocatalytic activity of Bi_2O_3 prepared by different precipitants, *Adv. Matet. Res.*, **239-242**, 998 **(2011)**.

(Received 29th June 2020, accepted 27th August 2020)